Resource

Cell Reports

Macrophage Ontogeny Underlies Differences in Tumor-Specific Education in Brain Malignancies

Graphical Abstract

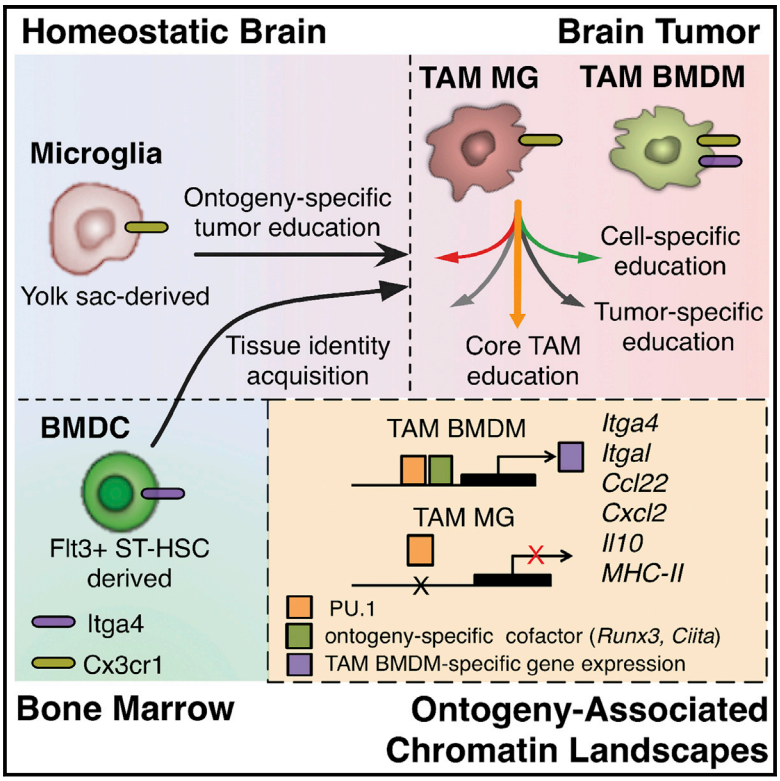

Highlights

- Peripherally derived macrophages (BMDMs) and microglia (MG) infiltrate brain tumors
- BMDMs and MG possess distinct transcriptional profiles and activation states in cancer
- Chromatin landscapes are distinct between BMDMs and MG
- CD49D is absent on MG and distinguishes them from BMDMs in mouse and human tumors

Authors

Robert L. Bowman, Florian Klemm, Leila Akkari, ..., Viviane Tabar, Philip H. Gutin, Johanna A. Joyce

Correspondence

johanna@joycelab.org

In Brief

Bowman et al. use genetic lineage tracing models to interrogate the ontogeny of tumor-associated macrophages in brain malignancy. These studies show that bone-marrow-derived macrophages (BMDMs) and tissue-resident microglia (MG) are present in glioma and brain metastases, possessing distinct transcriptional and chromatin states, and identify markers distinguishing these cell populations.

Accession Numbers

GSE86573

Bowman et al., 2016, Cell Reports *17*, 2445–2459
November 22, 2016
http://dx.doi.org/10.1016/j.celrep.2016.10.052

Cell Reports
Resource

Macrophage Ontogeny Underlies Differences in Tumor-Specific Education in Brain Malignancies

Robert L. Bowman,[1,2] Florian Klemm,[1,3,4] Leila Akkari,[1,3,4] Stephanie M. Pyonteck,[1] Lisa Sevenich,[1] Daniela F. Quail,[1] Surajit Dhara,[5] Kenishana Simpson,[1] Eric E. Gardner,[6] Christine A. Iacobuzio-Donahue,[5,7] Cameron W. Brennan,[8] Viviane Tabar,[8] Philip H. Gutin,[8] and Johanna A. Joyce[1,3,4,9,*]
[1]Cancer Biology and Genetics Program
[2]Gerstner Sloan Kettering Graduate School of Biomedical Science
Memorial Sloan Kettering Cancer Center, New York, NY 10065, USA
[3]Department of Oncology
[4]Ludwig Institute for Cancer Research
University of Lausanne, 1066 Lausanne, Switzerland
[5]Human Oncology and Pathogenesis Program
[6]Molecular Pharmacology Program
[7]Department of Pathology
[8]Department of Neurosurgery
Memorial Sloan Kettering Cancer Center, New York, NY 10065, USA
[9]Lead Contact
*Correspondence: johanna@joycelab.org
http://dx.doi.org/10.1016/j.celrep.2016.10.052

SUMMARY

Extensive transcriptional and ontogenetic diversity exists among normal tissue-resident macrophages, with unique transcriptional profiles endowing the cells with tissue-specific functions. However, it is unknown whether the origins of different macrophage populations affect their roles in malignancy. Given potential artifacts associated with irradiation-based lineage tracing, it remains unclear if bone-marrow-derived macrophages (BMDMs) are present in tumors of the brain, a tissue with no homeostatic involvement of BMDMs. Here, we employed multiple models of murine brain malignancy and genetic lineage tracing to demonstrate that BMDMs are abundant in primary and metastatic brain tumors. Our data indicate that distinct transcriptional networks in brain-resident microglia and recruited BMDMs are associated with tumor-mediated education yet are also influenced by chromatin landscapes established before tumor initiation. Furthermore, we demonstrate that microglia specifically repress *Itga4* (CD49D), enabling its utility as a discriminatory marker between microglia and BMDMs in primary and metastatic disease in mouse and human.

INTRODUCTION

Macrophages are terminally differentiated cells of the myeloid lineage, with critical functions in tissue development and homeostasis (Okabe and Medzhitov, 2016). These cells serve as a nexus between adaptive and innate immunity, regulating responses to inflammation and wound healing (Mosser and Edwards, 2008). To facilitate these diverse functions, macrophages employ considerable plasticity in response to a range of cytokines. These responses fall within a spectrum of different phenotypes ranging from classically activated pro-inflammatory macrophages to alternatively activated anti-inflammatory macrophages (Xue et al., 2014). Macrophages also possess substantial diversity and plasticity, with recent studies revealing important insights into the developmental origins of tissue-resident macrophages and uncovering tissue-specific gene expression patterns and enhancer landscapes (Gautier et al., 2012; Ginhoux et al., 2010; Gomez Perdiguero et al., 2015; Lavin et al., 2014; Mass et al., 2016).

While the local tissue environment sculpts macrophage transcriptional profiles and epigenetic states in homeostasis (Lavin et al., 2014), it is unknown whether an inflammatory tissue environment may promote differences between macrophage populations of distinct ontogenies. This is particularly relevant in cancer, where tumor-associated macrophages (TAMs) are derived from monocytes and also potentially from tissue-resident macrophages (Du et al., 2008; Pyonteck et al., 2013; Solga et al., 2015).

Brain-resident macrophages, microglia (MG), develop from erythromyeloid precursors in the yolk sac (Gomez Perdiguero et al., 2015; Kierdorf et al., 2013a; Schulz et al., 2012). Unlike other tissue-resident macrophages, during homeostasis, MG undergo self-renewal and their pool is not replenished by monocytes (Ajami et al., 2007). Microglia are also resistant to myeloablative irradiation (Kennedy and Abkowitz, 1997). Indeed, this property has been used extensively in bone marrow transplantation (BMT) models to distinguish radio-resistant MG from BM-derived macrophages (BMDMs) (Huang et al., 2014; Sedgwick et al., 1991). However, only under conditions of blood-brain

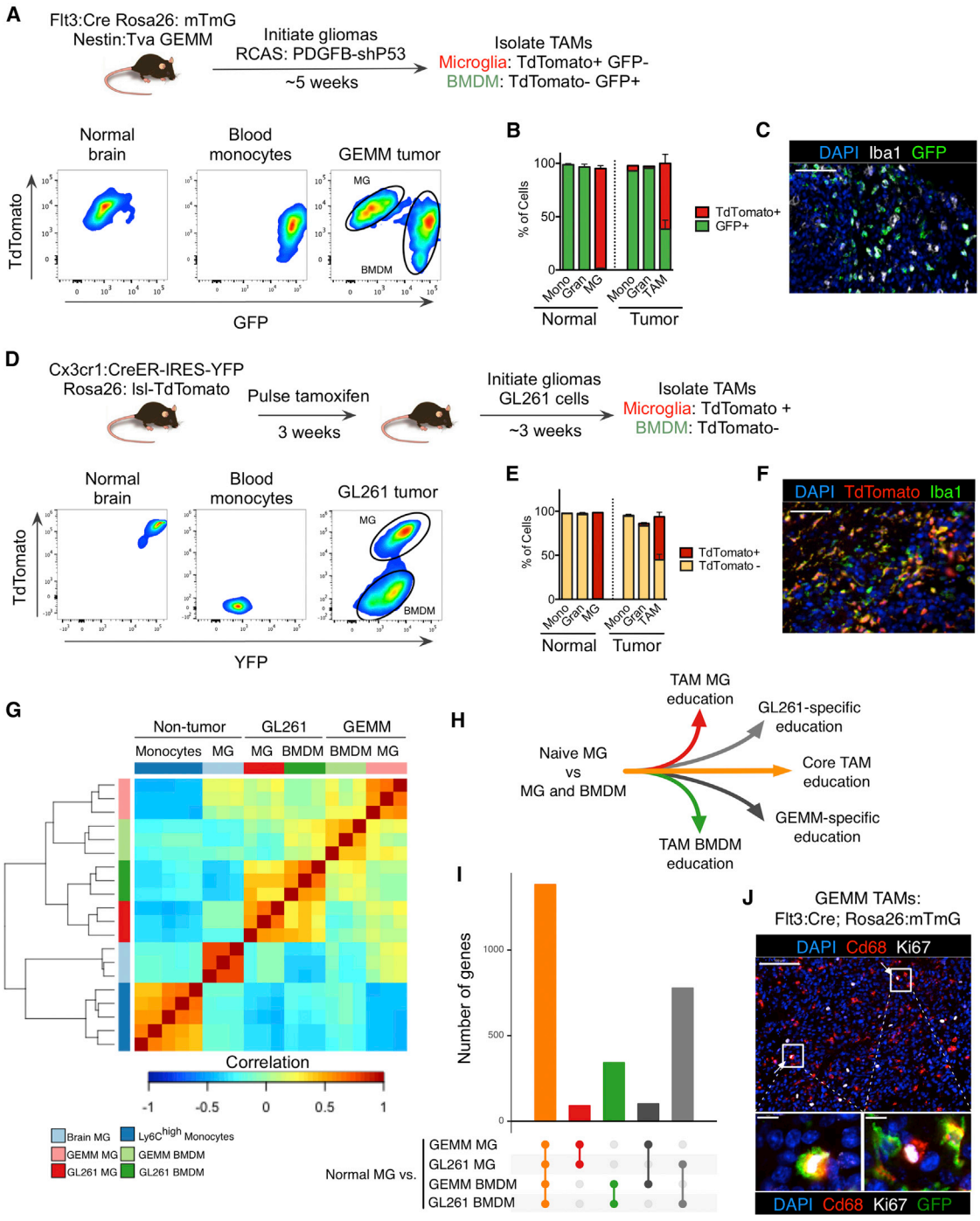

Figure 1. Lineage Tracing Systems Demonstrate Heterogeneity in TAM Ontogeny in Multiple Models of Glioma

(A) Experimental scheme for the GEMM-shP53 model (see Supplemental Experimental Procedures for details). Representative flow cytometry panels for TdTomato and GFP are shown for $Cd45^+Cd11b^+Ly6G^-Ly6C^-$ microglia (MG), $Cd45^+Cd11b^+Ly6G^-Ly6C^+$ monocytes, and $Cd45^+Cd11b^+Ly6G^-Ly6C^-$ TAMs from GEMM-shP53 gliomas.

(B) Quantitation of $TdTomato^+$ and GFP^+ monocytes (Mono) and granulocytes (Gran) in peripheral blood, MG in non-tumor-bearing brain, and monocytes, granulocytes, and TAMs in GEMM-shP53 gliomas as depicted in (A). Bars represent mean and SEM (n = 3–5 for each group).

(C) Representative immunofluorescence (IF) staining of Iba1 (white), GFP (green), and DAPI (blue) in a GEMM-shP53 tumor as depicted in (A). Scale bar, 50 μm. Data are representative of n = 5 tumors.

(D) Experimental design for Cx3cr1 lineage-tracing model (see Experimental Procedures for details). Monocytes, MG, and TAMs were isolated as described in (A) and evaluated for TdTomato and YFP reporter expression. Data are representative of n = 3 mice.

(legend continued on next page)

barrier (BBB) disruption (e.g., via irradiation [IR] or chemical manipulation) does there appear to be a significant contribution of BMDMs to the brain macrophage pool in a non-pathological context (Bruttger et al., 2015; Mildner et al., 2007). This is relevant to brain tumors such as gliomas, where there is also disruption of the BBB with disease progression (Dubois et al., 2014). IR-BMT has shown BMDM abundance in murine CNS cancers (Biffi et al., 2004; De Palma et al., 2005; Huang et al., 2014; Müller et al., 2015; Pyonteck et al., 2013); however, given the current lack of markers definitively distinguishing MG and BMDMs, it remains unclear if BMDM recruitment indeed occurs in brain tumors in the absence of irradiation. The need for markers distinguishing these cells is especially critical in human disease, where lineage tracing is not possible.

Here, we utilize multiple genetic lineage tracing models to demonstrate that BMDMs are indeed present in murine brain tumors. Gene expression profiling showed that while BMDMs and MG share features of tumor education, they also exhibit distinct activation modes. Our data suggest these faculties are a result of inherent transcriptional networks poised before the onset of tumorigenesis, where ontogeny pre-biases cells to engage in distinct macrophage activation states. Lastly, we identify markers that distinguish MG and peripherally derived macrophages under homeostasis, as well as in glioma and brain metastasis in both mice and humans.

RESULTS

Tumor-Associated BMDMs Are Present in Mouse Glioma Models

To track the ontogeny of myeloid cells in murine gliomas, we utilized a hematopoietic lineage tracing system, Flt3:Cre; Rosa26:mTmG, which has been used to show that peripheral myeloid cells develop from Flt3$^+$ short-term hematopoietic stem cells (ST-HSCs) and are GFP$^+$, while parenchymal MG develop independently of ST-HSC precursors and are thus negative for the GFP reporter, remaining TdTomato$^+$ (Boyer et al., 2011; Gomez Perdiguero et al., 2015). In non-tumor-bearing mice, >98% of blood monocytes were GFP$^+$, and <1% of MG showed recombination for the mTmG reporter (Figure 1A). The spleen was composed of GFP$^+$ lymphocyte-rich follicles, surrounded by TdTomato$^+$ stromal cells, while the brain parenchyma did not contain any detectable GFP$^+$ cells (Figure S1A).

We next bred this line to the nestin:Tva (nTva) line to trace myeloid cell ontogeny in a genetically engineered mouse model (GEMM) of glioma. We induced gliomas by intracranial injection of DF1 cells transfected with RCAS vectors encoding platelet-derived growth factor β (PDGFB) and a short hairpin against P53 (Ozawa et al., 2014) (Figure 1A), termed GEMM-shP53 herein. Flow cytometry of end-stage gliomas demonstrated that all monocytes (Cd45$^+$Cd11b$^+$Ly6C^{high}Ly6G$^-$) and granulocytes (Cd45$^+$Cd11b$^+$Ly6C^{low}Ly6G^{high}) in the tumor were GFP$^+$ (Figure 1B), while the bulk TAM compartment (Cd45$^+$Cd11b$^+$Ly6C$^-$Ly6G$^-$) was composed of both GFP$^+$ TAM BMDMs and GFP$^-$ TAM MG (Figures 1A, 1B, and S1B), confirmed by tissue immunofluorescence (IF) co-staining with the pan-macrophage marker Iba1 (Figure 1C). By contrast, the contralateral, non-malignant brain contained only GFP$^-$ MG, demonstrating the specific abundance of TAM BMDMs only within the tumor mass (Figure 1B).

We and others have utilized IR-BMT to show that TAM BMDMs are recruited to murine gliomas (Huang et al., 2014; Pyonteck et al., 2013). However, IR can lead to ectopic recruitment of BMDMs to the brain and thereby increase their relative abundance (Müller et al., 2015). We verified these findings in the orthotopic, syngeneic GL261 glioma model and found the TAM compartment was composed of both TAM MG and TAM BMDMs using both IR-BMT lineage tracing and IR-independent Flt3:Cre lineage tracing (Figures S1C and S1D). TAM BMDM abundance was significantly increased in the IR-BMT model compared to the Flt3:Cre model (Figure S1D), reinforcing previous reports that IR-BMT can skew the ratio of MG and BMDMs. Critically, however, using Flt3:Cre lineage tracing, we found that BMDMs composed >35% of the bulk TAM population in gliomas without IR preconditioning, demonstrating that BMDM infiltration into tumors is not solely an artifact of IR (Figure S1D).

To exclude the possibility that this finding was due to a subset of TAM MG spontaneously upregulating *Flt3* expression, we utilized a complementary lineage-tracing approach previously indicated to be specific for MG in the normal brain: Cx3cr1:CreER-IRES YFP; Rosa26:lsl-TdTomato (see Supplemental Experimental Procedures for details) (Parkhurst et al., 2013). 3 days after tamoxifen-induced labeling, >99% of MG and circulating monocytes were TdTomato$^+$ (Figure S1E). However, after 3 weeks, blood monocytes no longer retained the TdTomato$^+$ reporter, indicating their turnover and replenishment by tamoxifen-"naive" monocytes (Figure S1E). By contrast, >99% of MG remained TdTomato$^+$ (Figure S1E). We induced GL261 tumors in these mice, at 7 weeks of age, and observed both TdTomato$^+$ TAM MG and TdTomato$^-$ TAM BMDMs (Figures 1D and 1E). Meanwhile, all monocytes and granulocytes were TdTomato$^-$ in the tumor and periphery (Figure 1E). These findings were substantiated by IF co-staining of tissue

(E) Flow cytometry quantitation of TdTomato$^+$ and TdTomato$^-$ monocytes and granulocytes in peripheral blood, MG in non-tumor-bearing brain, and monocytes, granulocytes, and TAMs in GL261 gliomas as depicted in (D). Bars represent mean and SEM (n = 3 for each group).
(F) Representative IF staining for Iba1 (green), TdTomato (red), and DAPI (blue) in a GL261 tumor. Scale bar, 50 μm.
(G) Pairwise correlation matrix of normalized RNA-seq counts from monocytes (n = 5), normal MG (n = 3), and the four TAM populations from the different models: GEMM-shP53 TAM MG, GEMM-shP53 TAM BMDMs, GL261 TAM MG, and GL261 TAM BMDMs (n = 3 for each group).
(H) Diagram depicting different modules of TAM education compared to normal MG.
(I) Differentially expressed genes between normal MG and the four TAM populations were tabulated. Bar chart depicts the number of differentially expressed genes shared between the different groups.
(J) Representative IF staining of Ki67$^+$ TAM BMDMs and TAM MG in the GEMM-shP53 model as depicted in (A) (Ki67, white; CD68, red; DAPI, blue; and GFP, green; omitted from top panel). Scale bars represent 100 μm (top panel) and 10 μm (lower panels). Data are representative of n = 5 tumors.

sections with Iba1 (Figure 1F). Importantly, there was a gradient of eYFP reporter expression levels, with highest expression in TdTomato$^+$ TAM MG, slightly lower levels in TdTomato$^-$ TAM BMDMs, and lowest levels in monocytes (Figure S1F), demonstrating the capacity of TAM BMDMs to express *Cx3cr1* in brain tumors. Thus, *Cx3cr1* expression alone cannot be used to strictly identify MG in gliomas. Together, these complementary genetic lineage-tracing models show that BMDMs contribute to the TAM pool in several murine models of glioma, in the absence of IR.

RNA Sequencing Reveals Multimodal Patterns of TAM Education

We next analyzed the transcriptional profiles of TAM MG and TAM BMDMs in gliomas. We performed RNA-sequencing (RNA-seq) on sorted populations of TAM MG and TAM BMDM from GEMM-shP53 and GL261 tumors using the Flt3-based and Cx3cr1-based lineage tracing systems, respectively. We also collected MG and Ly6C^{high} blood monocytes from non-tumor-bearing Flt3:Cre Rosa26:mTmG mice. Global correlation analyses revealed distinct clustering of all TAM populations from normal MG and monocytes, with further cell-type-specific and tumor-specific clustering (Figure 1G). As expected, monocytes were enriched for *Ly6c2* expression, while both TAM MG and TAM BMDMs expressed higher levels of macrophage differentiation markers (e.g., *Aif1* and *Mertk)* than monocytes (Figure S1G). Normal MG and TAM MG expressed higher levels of MG-enriched genes (e.g., *Cx3cr1*, *P2ry12*, and *Tmem119*) than monocytes and TAM BMDMs (Figure S1G).

We next delineated cell-type-specific, tumor-specific, and conserved patterns of tumor education among TAMs (Figure 1H). We identified differentially expressed genes between each TAM population from GEMM-shP53 and GL261 tumors compared to normal MG and monocytes (Figures 1I and S1H; Table S1A). Using normal MG as the reference, we found 91 genes specifically upregulated in TAM MG from both GEMM-shP53 and GL261 models (Figure 1I, red bar), and 342 genes upregulated in TAM BMDMs from both GEMM-shP53 and GL261 models (Figure 1I, green bar). We also identified genes that were specifically upregulated in TAM MG and TAM BMDMs from either the GEMM-shP53 (n = 102) or GL261 (n = 778) models. The largest gene set (n = 1383) was significantly upregulated in all TAM populations compared to normal MG (Figure 1I, orange bar). Similar patterns of expression were observed when monocytes were used as the reference population (Figure S1H; Table S1B).

Many cell-cycle-related genes were upregulated, suggesting increased TAM proliferation compared to normal MG and monocytes (Tables S1A and S1B). Indeed, we found Ki67$^+$ cells in both Iba1$^+$GFP$^+$ TAM BMDM and Iba1$^+$GFP$^-$ TAM MG in the Flt3-based lineage-tracing model (Figure 1J). Conserved upregulation of complement-related factors, extracellular matrix components, proteases, lipid metabolism mediators, and clotting factors were also evident in both TAM populations (Table S1A). In addition to these programmatic changes, compared to normal MG, there was upregulation of growth factors (*Igf1*, *Areg*, and *Osm)*, chemokines and cytokines (*Spp1*, *Ccl5*, *Cxcl9*, and *Cxcl10)*, and other immune modulators, including *Cd274*/PD-L1 and major histocompatibility complex (MHC class) I molecules (*H2-K1*, *H2-D1*, and *B2m*) (Table S1A). A similar distribution of differentially expressed genes was evident in comparing the TAM populations from both glioma models to blood monocytes (Figure S1H; Table S1B). Interestingly, we found several MG-enriched genes (e.g., *Tmem119*, *Olfml3*, *Lag3*, *Jam2*, and *Sparc*) (Gautier et al., 2012) enriched in TAM BMDMs in both GL261 and GEMM-shP53 models compared to monocytes (Table S1B). Despite this difference, there was still higher expression of MG-related genes in normal MG and TAM MG than in TAM BMDMs. Meanwhile, other MG-enriched genes showed no such induction in TAM BMDMs (*P2ry12, Sall1*, and *Mef2c*). Collectively, these data are consistent with *Cx3cr1* upregulation specifically in gliomas (Figure S1F) and the notion that macrophages acquire tissue-resident gene expression upon infiltration into a foreign tissue (Gosselin et al., 2014; Lavin et al., 2014).

TAM BMDMs and TAM MG Possess Distinct Education Patterns

We investigated transcriptional differences between TAMs derived from BMDMs versus MG and identified 378 differentially expressed genes enriched in TAM MG compared to TAM BMDMs in both GEMM-shP53 and GL261 models and 485 genes enriched in TAM BMDMs compared to TAM MG (Figure 2A; Table S2). As expected, among the 378 TAM MG genes, we found markers previously shown to be enriched in MG compared to other macrophage populations, including *P2ry12*, *Tmem119*, *Slc2a5*, *Pros1*, and *Sall1* (Figure 2A) (Gautier et al., 2012). Consistent with their tissue-specific functions, we found that normal MG and TAM MG were enriched for *Jam2* and *Ocln* (Figure S2A; Table S2), integral components of the blood-brain barrier (Liu et al., 2012). Similarly, TAM MG expressed higher levels of classical complement factors *C4b*, *C2*, and *Cfh* (Figure S2A), a pathway important for MG function in synaptic pruning and host defense (Stephan et al., 2012).

Meanwhile, TAM BMDMs expressed high levels of alternative complement cascade components *Cfb* and *Cfp* (Figure S2A) and enrichment of many immune effectors, including *Cd40*, *Jak2*, *Ifitm1*, *Ifitm2*, *Tlr11*, *Tlr5*, *Tlr8*, *Mefv*, and *Fas* (Figure S2A). In the GEMM-shP53 model, interleukin 1 (IL-1) pathway ligands were differentially expressed, with *Il1a* enriched in TAM MG and *Il1b* in TAM BMDMs, and similar trends were observed in the GL261 model (Figure S2B). While *Il1r1* levels did not significantly differ, TAM BMDMs expressed higher levels of the IL-1 signaling antagonist *Il1rn*, and the IL-1 decoy receptor *Il1r2* (Figure S2B). These results complement reports in non-cancer contexts demonstrating *Il1a* enrichment in MG compared to BMDMs, where IL-1 signaling played a critical role in MG repopulation and maintenance (Bruttger et al., 2015).

We next interrogated chemokines, growth factors, and immune modulators associated with different macrophage activation states. In addition to model-specific gene expression changes (Figure S2C; Table S3), we found in both GEMM and GL261 models that TAM BMDMs were enriched for chemokines involved in wound healing, including *Ccl22*, *Ccl17*, *Cxcl2*, *Cxcl3*, and *Cxcl16* (Figure 2B) (Xue et al., 2014). Interestingly, TAM MG were enriched for expression of *Ccl4* and *Tnf*, chemokines associated with a pro-inflammatory response (Xue et al., 2014). This difference in activation states was supported by a programmatic increase in antigen presentation centered on increased expression

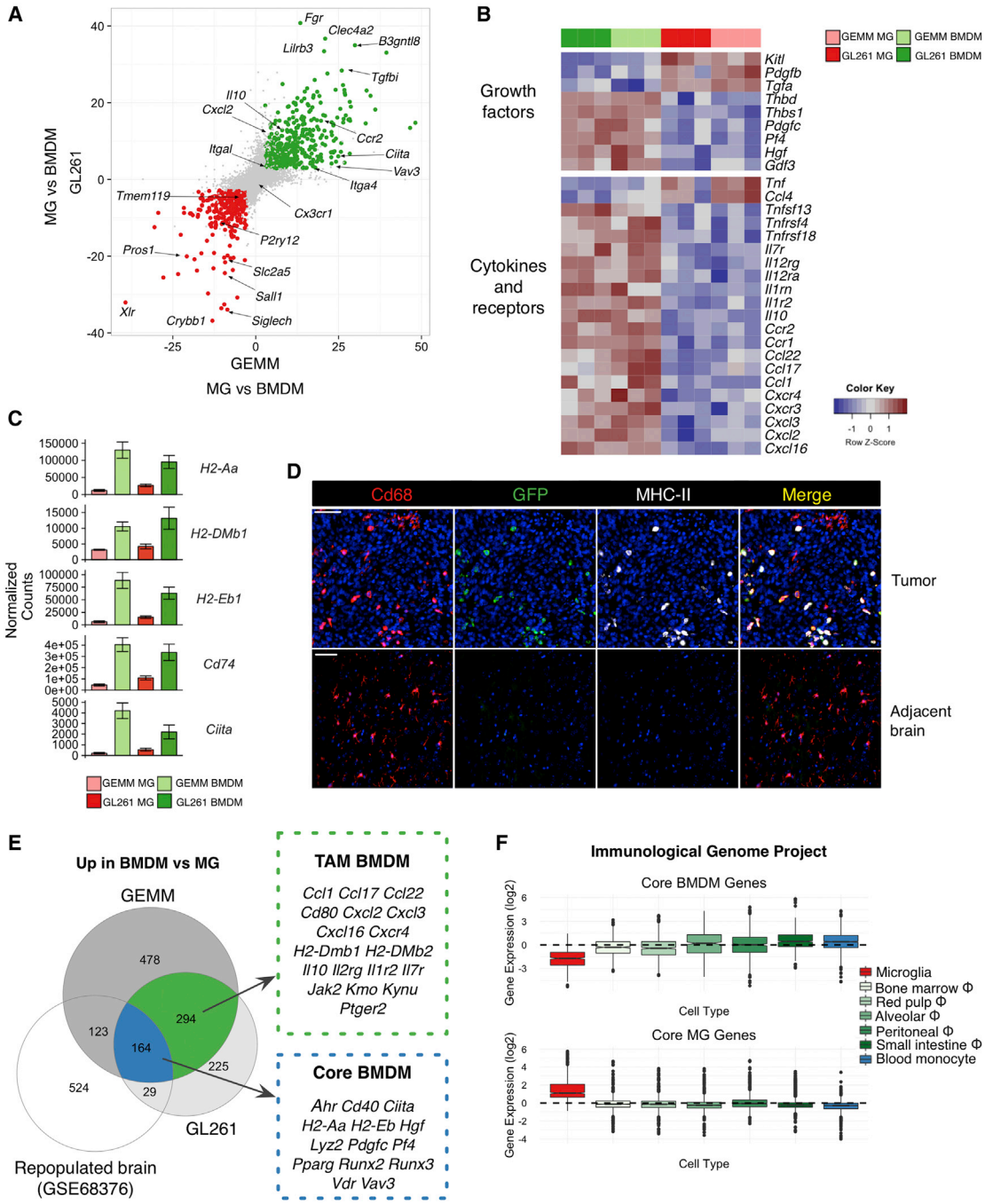

Figure 2. TAM BMDMs and TAM MG Possess Distinct Gene Expression Patterns

(A) Scatterplot depicting −log10 (p value) × sign (fold change) between TAM BMDMs and TAM MG in GEMM-shP53 gliomas (x axis) and GL261 gliomas (y axis). Significantly upregulated genes (log2 fold change of more than ±1 and FDR < 1%) are in green for BMDM and red for MG.

(B) Heatmap depicting row-normalized log2 gene expression values for indicated genes in GL261 TAM BMDMs (dark green), GEMM-shP53 TAM BMDMs (light green), GL261 TAM MG (dark red), and GEMM-shP53 TAM MG (light red).

(C) Bar plots depicting normalized gene expression values for indicated genes in these four different TAM populations. Bars represent mean ± SEM.

(D) Representative IF staining in GEMM-shP53 Flt3:Cre Rosa26:mTmG gliomas and adjacent normal brain for Cd68 (red, Alexa Fluor 594), GFP (green), and MHC II (white). DAPI is shown in blue, and TdTomato fluorescence is not shown. Scale bar, 100 μm. Data are representative of n = 5 tumors.

(E) Venn diagram depicting significantly upregulated genes in BMDMs versus MG in GL261 model, GEMM-shP53, and non-malignant brain (GSE68376 dataset). Select genes are listed.

(F) Boxplot of core BMDM genes (Figure 2E) and core MG genes (Figure S2D), where each data point represents the *Z* scored expression of a gene across the indicated cell populations using available datasets from the Immunological Genome Project.

of the MHC II master regulator *Ciita* (Reith et al., 2005) and its transcriptional targets *H2-Aa*, *H2-DMb1*, *H2-Eb1*, and *Cd74* in TAM BMDMs (Figure 2C). IF staining in Flt3:Cre; GEMM-shP53 tumors revealed a marked increase in MHC II in tumors, compared to adjacent brain, restricted to GFP$^+$ TAM BMDMs (Figure 2D). In addition to this antigen-presentation program, costimulatory molecules such as *Cd80*, *Cd40*, and *Cd200r4* were increased (Figure S2A). These findings were further complemented by TAM BMDM-enriched expression of the Aryl-hydrocarbon receptor (*Ahr*), a transcription factor previously shown to mediate immune suppression (Murray et al., 2014; Opitz et al., 2011) (Figure S2A). Critically, we also found that the immunosuppressive cytokine *Il10* was enriched in TAM BMDMs compared to TAM MG (Figure 2B). Collectively, these results suggest that TAM BMDMs engage in a chronic wound-healing-like state reminiscent of an alternatively activated macrophage (Mosser and Edwards, 2008). Similar phenotypes have been shown in models of oligodendrocyte cell death, where, despite high MHC II expression, myeloid cells did not activate a robust T cell response (Locatelli et al., 2012), suggestive of a tolerogenic program.

We next asked if the differences in inflammatory mediators were an inherent feature of BMDMs upon entry into the brain or rather a consequence of tumor education. Previous studies demonstrated that when MG are depleted and the brain preconditioned by IR, BMDMs can seed the brain and contribute significantly to the brain macrophage pool (hereafter termed "ectopic BMDM" in a normal "repopulated brain") (Bruttger et al., 2015). We used this dataset for comparative analyses with our TAM BMDMs and TAM MG RNA-seq data to discriminate tumor education differences from ontogenetic, non-tumor-associated differences. This juxtaposition allowed us to identify genes enriched in TAM MG versus TAM BMDMs as well as normal MG versus "ectopic" BMDMs. These "core" MG genes included not only known MG markers such as *Jam2*, *Siglech*, and *P2ry12* but also complement factors *C2*, *C4b*, and *Cfh* as well as the pro-inflammatory cytokines *Ccl4* and *Tnf* (Figure S2D, n = 245 genes; Table S4). We identified genes enriched in TAM BMDMs (n = 294) specifically in the context of a tumor, including *Il10*, *Cxcl2*, *Cxcl3*, *Ccl17*, *Ccl22*, and *H2-Dmb1* (Figure 2E). In contrast to this tumor-specific expression profile, there were also 164 core BMDM genes enriched in BMDM compared to MG, regardless of the presence or absence of a tumor, including *Ciita*, *Ahr*, *Runx2*, *Runx3*, *Vav3*, and *Vdr* (Figure 2E; Table S4). These data indicate some features distinguishing TAM BMDMs and TAM MG are inherent to their differential ontogenies, while others are only acquired upon interaction with, and education by, the tumor microenvironment.

As many of the core BMDM genes are central players in innate immunity, we queried the immunological genome project database to determine if these genes were over-represented in any particular myeloid cell population. Interestingly, we found that these genes were actually repressed in MG compared to tissue-resident macrophages of the BM, spleen, lung, peritoneum, small intestine, and monocyte progenitors (Figure 2F). Meanwhile, core MG genes were indeed enriched in MG compared to other myeloid cells (Figure 2F). These data suggest that core BMDM genes are not specifically enriched in TAM BMDMs or macrophages in general but are specifically repressed in MG.

Recent studies have highlighted extensive epigenetic diversity among tissue-resident macrophages (Lavin et al., 2014); thus, we hypothesized that the MG-repressed genes may be epigenetically altered in MG compared to even the distantly related monocytes. Indeed, when we analyzed these published datasets, we observed increased H3K27 acetylation in the promoters of normal monocytes compared to normal MG for the core BMDM genes (Figure S2E). Similarly, there was increased H3K27 acetylation in the promoters of core MG genes in MG compared to monocytes (Figure S2E). Enhancer specification and epigenetic states in MG and other macrophage populations have been associated with differential PU.1 occupancy. Interrogating previously published data (Gosselin et al., 2014), we observed that several macrophage subsets (including BMDM) all showed increased PU.1 binding at the promoters of our core BMDM genes compared to normal MG (Figure S2F). Meanwhile, variability in PU.1 occupancy was minimal at the promoters of core MG genes (Figure S2F). Similar binding dynamics were evident in enhancer elements, where PU.1 occupancy in enhancer regions of core BMDM genes was higher in BMDMs than MG, with less pronounced differences present in core MG genes (Figure S2G). Thus, epigenetic landscapes established before the development of a tumor may play a role in regulating differential activation patterns subsequently observed in malignancy.

Identification of Transcription Factor Networks Underlying TAM Activation

Given the epigenetic differences in the non-malignant setting, we next determined if chromatin states also differed between TAM BMDMs and TAM MG. We performed assay for transposase-accessible chromatin sequencing (ATAC-seq) (Buenrostro et al., 2013) to assess chromatin accessibility in TAM BMDMs and TAM MG sorted from the GL261 model (Figure 1D). We found the ATAC-seq signal was associated with cell-type-specific gene expression. In TAM BMDMs, the promoters of core BMDM and TAM BMDM genes had higher ATAC-seq signal than core MG and TAM MG genes, while TAM MG promoters of core MG and TAM MG genes had a higher ATAC-seq signal than core BMDM and TAM BMDM genes (Figure S3A). Within enhancers and intronic elements of these gene sets, we identified 120 BMDM-specific peaks in TAM BMDM genes, including *Vav3*, and 704 MG-specific peaks in TAM MG genes, including *P2ry12* and *Sall1* (Figures 3A, S3B, and S3C; Table S5A).

We analyzed the transcription factor (TF) landscape underlying these different peaks and performed de novo motif analysis (motifs are shown in all capital letters). Motif analysis of these peaks revealed an enrichment of FOS/JUN and PU.1 binding sites in both TAM BMDM and TAM MG peaks (Figure 3B; Table S5B), reinforcing previous analyses demonstrating the critical role of PU.1 in establishing specific enhancer landscapes in tissue-resident macrophages (Gosselin et al., 2014). Besides these shared enrichments, we found TAM BMDM peaks enriched for RUNX and CREB/bZIP motifs, while TAM MG peaks were enriched for SMAD3 and MEF2A motifs (Figure 3B).

To determine if these motifs reflected pathway activation of particular TFs we modeled the expression of their predicted downstream targets (see Supplemental Experimental Procedures). We identified TF families with enriched activity in TAM

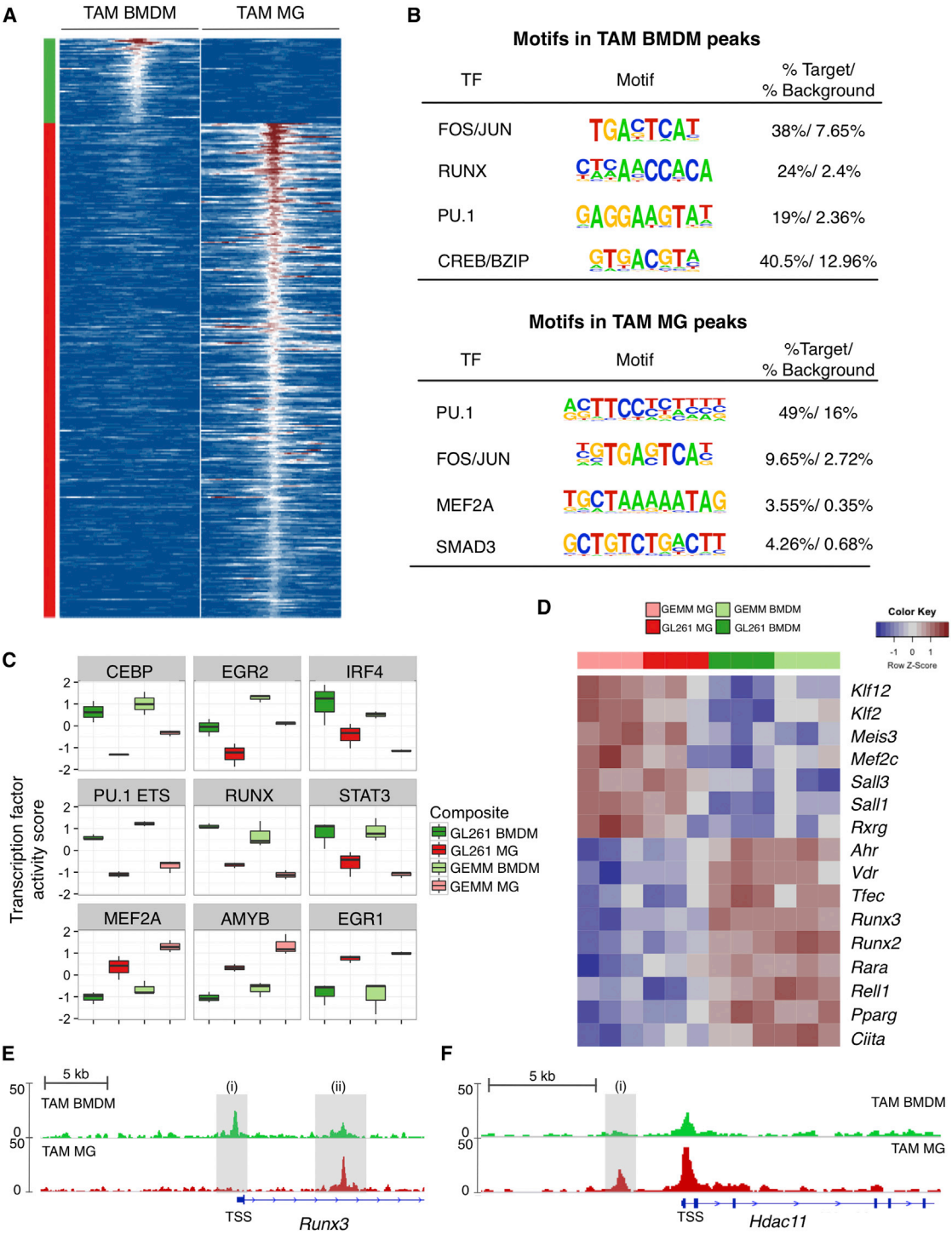

Figure 3. Cell-Specific Transcription Factor Activities Underlie Differences between TAM BMDMs and TAM MG

(A) Heatmap depicting ATAC-seq signal 1 kb upstream and downstream of peaks specifically enriched in GL261 TAM BMDMs (left) and GL261 TAM MG (right). Peaks were selected based on association with differentially expressed genes between TAM BMDMs (top, green) and TAM MG (bottom, red).

(B) Motifs identified by HOMER to be enriched in TAM BMDM and TAM MG peaks shown in (A).

(C) Boxplots depicting normalized TF activity scores for indicated motifs across TAM BMDMs and TAM MG from GL261 and GEMM-shP53 gliomas.

(D) Heatmap depicting row-normalized log2 gene expression values for indicated genes in four different TAM populations.

(E and F) ATAC-sequencing tracks from TAM BMDMs (top, green) and TAM MG (bottom, red) from GL261 gliomas for (E) *Runx3* and (F) *Hdac11*. Shaded gray regions indicate peaks specifically referenced in text. The y axis values indicate tags per 10,000,000 with a range of 0–50. TSS denotes transcription start site.

BMDMs relative to TAM MG in the GEMM-shP53 and GL261 models (and vice versa) (Figures 3C and S3D). Among a panel of different TFs, EGR1 and MEF2A were enriched in TAM MG (Figures 3C and S3D; Table S5C). Interestingly, MEF2 is associated with MG identity (Lavin et al., 2014). In TAM BMDMs, TF motifs involved in monocyte to macrophage differentiation were enriched, including RUNX, CEBP, and PU.1 (Figures 3C and S3D) (Alder et al., 2008). STAT3 and IRF4 were also enriched (Figure 3C), both of which have been associated with differential functions in macrophage activation (Mosser and Edwards, 2008; Ostuni and Natoli, 2011). We complemented these genome-wide TF activity analyses with motif enrichment analysis on the promoters of TAM BMDM-specific and TAM MG-specific genes using HOMER (Heinz et al., 2010) (Figure S3E). This also revealed an enrichment of MEF2 motifs in TAM MG, demonstrating the consistent role of tissue-specific transcriptional programs in TAM MG education. Meanwhile, TAM BMDM-specific genes were again enriched in PU.1, RUNX, and CEBP motifs (Figure S3E). These findings were further corroborated by increased expression of brain-specific TFs (*Mef2c*, *Sall1*, and *Sall3)* in TAM MG, while TAM BMDMs were enriched for *Ciita*, *Vdr*, *Ahr*, and *Runx* family members (Figure 3D; Table S2A).

Given the consistent enrichment of RUNX activity in TAM BMDMs, we next focused on examining the expression and chromatin state of *Runx* family members. *Runx2* and *Runx3* were enriched in TAM BMDMs compared to TAM MG (Figure 3D). While no differences were found in the chromatin state of *Runx1* or *Runx2*, in the first intron of *Runx3* (Figure 3E, ii), we observed a peak present in TAM MG but reduced in TAM BMDMs (Figure 3E). Meanwhile, the *Runx3* promoter showed little open chromatin in TAM MG and a distinct peak in TAM BMDMs near the transcription start site (Figure 3E, i). Interestingly, both peaks have been shown to be transforming growth factor β (TGF-β)-responsive PU.1 binding sites associated with *Runx3* expression (Chopin et al., 2013), indicating the same signal transduction pathway can produce distinct outputs in TAM BMDMs and TAM MG.

We also identified enrichment of the epigenetic modifiers *Hdac7* and *Hdac9* in TAM BMDMs, while *Hdac11* was enriched in TAM MG (Figure S3F), the latter of which has been shown to repress *Il10* expression in macrophages (Villagra et al., 2009). Interestingly, an upstream enhancer element in *Hdac11* was significantly enriched in TAM MG compared to TAM BMDMs, a peak that contained a SMAD-responsive element (Figure 3F-i). Collectively, these results suggest that differential genomic PU.1 occupancy underlies distinct open chromatin states in BMDMs and MG, whereupon additional factors such as TGF-β/SMAD signaling and RUNX family members cooperate with PU.1 to enforce distinct transcriptional networks. Subsequent regulation of TFs and chromatin modifying factors, such as *Hdac11*, may explain the distinct cytokine expression patterns observed, such as TAM BMDM expression of *Il10* and TAM MG expression of *Tnf.*

Itga4/Cd49d Distinguishes Microglia and Peripherally Derived Macrophages in Murine Models of Brain Malignancy

We next sought to identify tools capable of distinguishing TAM BMDMs and TAM MG in human disease, where genetic lineage tracing is not possible. Given that TAM BMDMs in gliomas upregulated *Cx3cr1* (Figure S1F), a proposed MG marker, we sought to identify TAM BMDM-specific markers that instead remained silent in TAM MG. From the 164 core BMDM genes, we identified 40 candidate transmembrane proteins that might serve as useful markers for flow cytometry. Among these, the integrin subunit alpha 4, *Itga4*/Cd49d, emerged as a promising candidate, particularly given previous reports that it, along with the integrin subunit alpha L, *Itgal*/Cd11a, is regulated by RUNX family members, including *Runx1* and *Runx3* (Domínguez-Soto et al., 2005). Consistently, we found that *Itga4* and *Itgal* were specifically repressed in MG compared to other macrophage populations (Figure S4A). This was confirmed by flow cytometry, where Cd49d expression in MG was negligible or absent compared to macrophages of the spleen, liver, lung, bone marrow, and blood Ly6C$^+$ monocytes (Figure 4A). Ly6G$^+$ granulocytes were also Cd49d$^-$, which, along with Cd49d$^+$ lymphocytes in the Cd45$^+$Cd11b$^-$ gate, served as useful gating controls in subsequent experiments (Figure 4A).

We examined Cd49d and Cd11a expression in TAM BMDMs and TAM MG using Flt3:Cre-based lineage tracing in the GEMM-shP53 model. After gating on Cd45$^+$Cd11b$^+$Ly6C$^-$ Ly6G$^-$ cells, the normal brain only contained Cd45^{low}Cd49d$^-$ cells, and all peripheral monocytes were Cd45^{high}Cd49d$^+$ (Figure 4B). In tumors, we found two cell populations, Cd45^{low}Cd49d$^-$ and Cd45^{high}Cd49d$^+$, which contained GFP$^-$ TdTomato$^+$ MG and GFP$^+$ TdTomato$^-$ BMDMs, respectively (Figure 4B). Similar results were found for Cd11a (Figure 4B) and were replicated in the GL261 model using both Cx3cr1-based and Flt3:Cre lineage-tracing strategies (Figures S4B and S4C). Lastly, we evaluated Cd49d expression in a Pten loss-of-function PDGFB-driven glioma model (GEMM-*Pten^{Flox}*) where *Pten$^{Flox/Flox}$*; nTva$^+$ mice were injected with RCAS vectors encoding PDGFB and Cre (Huse et al., 2009). Using IR-BMT for lineage tracing, we found that Cd49d distinguishes donor and host-derived cells, including in glioma models with extended latency (~12 weeks for the GEMM-*Pten^{Flox}* model) (Figure S4D).

To evaluate other models of brain malignancy, we utilized an intracardiac injection model of brain metastasis (BrM) colonization using a tumor cell line (99LN-BrM). 99LN-BrM cells were originally derived from the lymph node of a MMTV:PyMT breast cancer GEMM and subjected to in vivo selection. We used this syngeneic, immunocompetent BrM model in conjunction with Cx3cr1-based lineage tracing and found that BrM lesions contained both TdTomato$^+$ Iba1$^+$ and TdTomato$^-$ Iba1$^+$ cells, indicating recruitment of both TAM MG and TAM BMDMs, respectively (Figures 4C and 4D). We validated these findings by flow cytometry, where Cd49d and Cd11a served as reliable markers of BMDMs as in the glioma models described above (Figure 4E). We again found that eYFP levels, a direct readout of *Cx3cr1* expression, were similar between TAM BMDMs and TAM MG in BrM, reinforcing the necessity of the Cx3cr1:CreER lineage tracing approach over that of the Cx3cr1 reporter (Figure S4E). Lastly, we confirmed these data in a well-established xenograft BrM model using brain homing MDA-MB-231 cells (Bos et al., 2009), in conjunction with IR-BMT lineage tracing using mRFP$^+$ donor cells. In this model, we identified two cell populations,

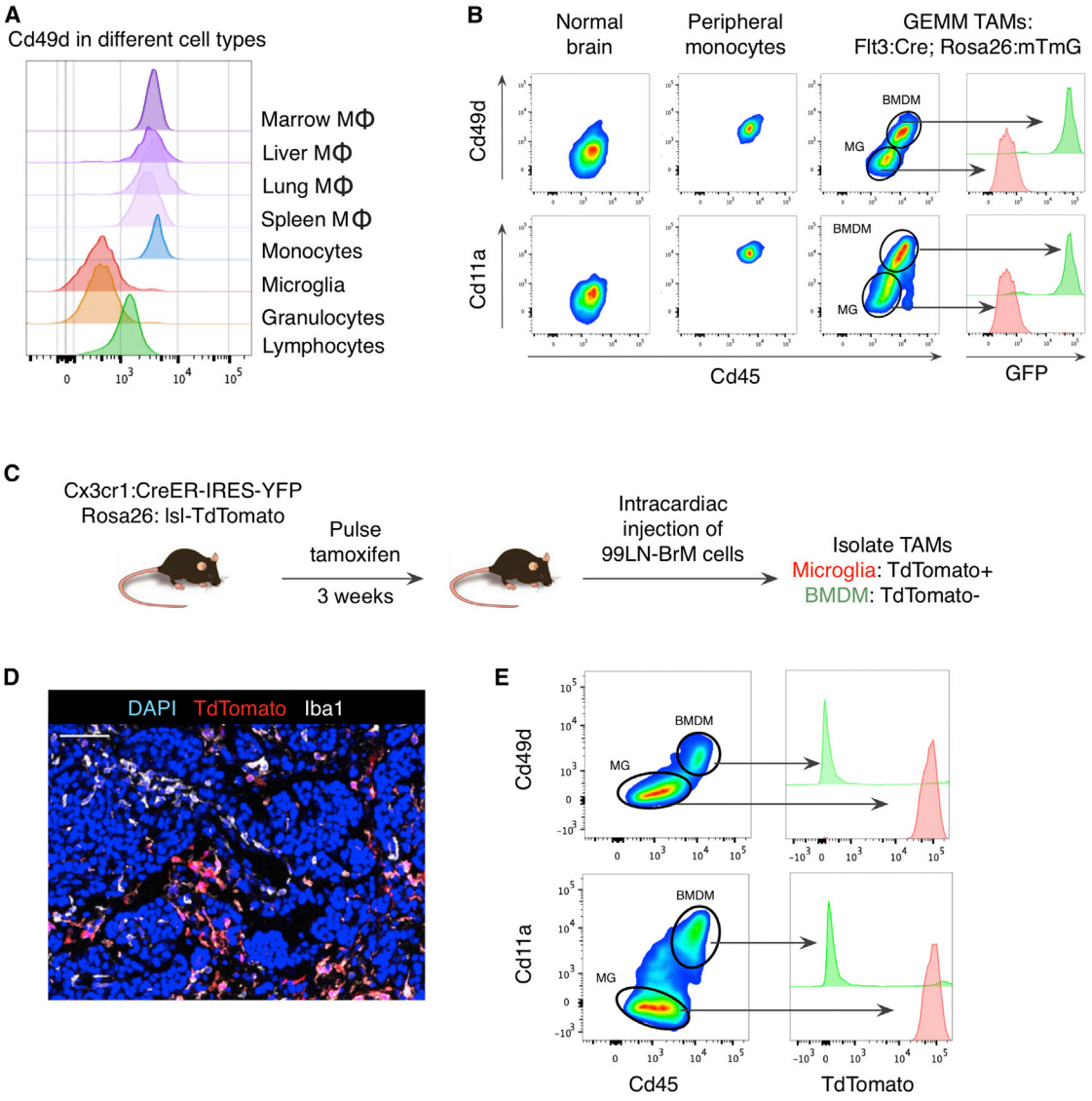

Figure 4. *Itga4*/Cd49d Distinguishes TAM BMDMs and TAM MG in Murine Brain Malignancy

(A) Histogram of Cd49d expression for indicated populations from non-tumor-bearing mice.

(B) Flow cytometry for Cd45 and either Cd49d (top) or Cd11a (bottom) in normal blood monocytes, normal MG (from adjacent normal brain), or TAMs isolated from Flt3:Cre Rosa26:mTmG mice with GEMM-shP53 tumors. Adjacent histograms indicate GFP expression in indicated populations.

(C) Experimental schematic for the 99LN-BrM model in Cx3cr1-lineage tracing mice.

(D) Representative IF staining of TdTomato (red), Iba1 (white), and DAPI (blue) 99LN-BrM tumors as depicted in (C). Scale bar, 50 μm.

(E) Flow cytometry as in (B) for the 99LN-BrM model, with TdTomato expression indicated in the adjacent histogram. Flow plots are representative of n = 5–8 mice.

$Cd45^{low}Cd49d^{-}$ MG and $Cd45^{high}Cd49d^{+}$ BMDM. The $mRFP^{+}$ donor cells were exclusively found within the $Cd45^{high}Cd49d^{+}$ BMDM gate (Figure S4F).

Together, our results obtained in multiple models of brain malignancy with distinct lineage-tracing approaches demonstrate that TAM BMDM accumulation is independent of BBB preconditioning by IR or intracranial injection. These data also thoroughly establish Cd49d as an efficient marker to distinguish resident MG and peripherally derived macrophages in homeostasis as well as in primary and metastatic brain malignancies.

CD49D Identifies Microglia and Macrophages in Human Brain Malignancies

We next investigated whether CD49D could be used to discriminate MG and peripherally derived macrophages in human brain tumors. We assessed CD49D expression by flow cytometry across a panel of surgical samples composed of non-malignant normal brain (n = 3), untreated high-grade glioma (GBM) (n = 3), lung adenocarcinomas (n = 6), and peripheral blood mononuclear cells (PBMCs) (n = 6). Consistent with our data in mice, granulocytes ($CD45^{+}CD11B^{+}CD66B^{+}CD14^{low}CD16^{+}$) did not

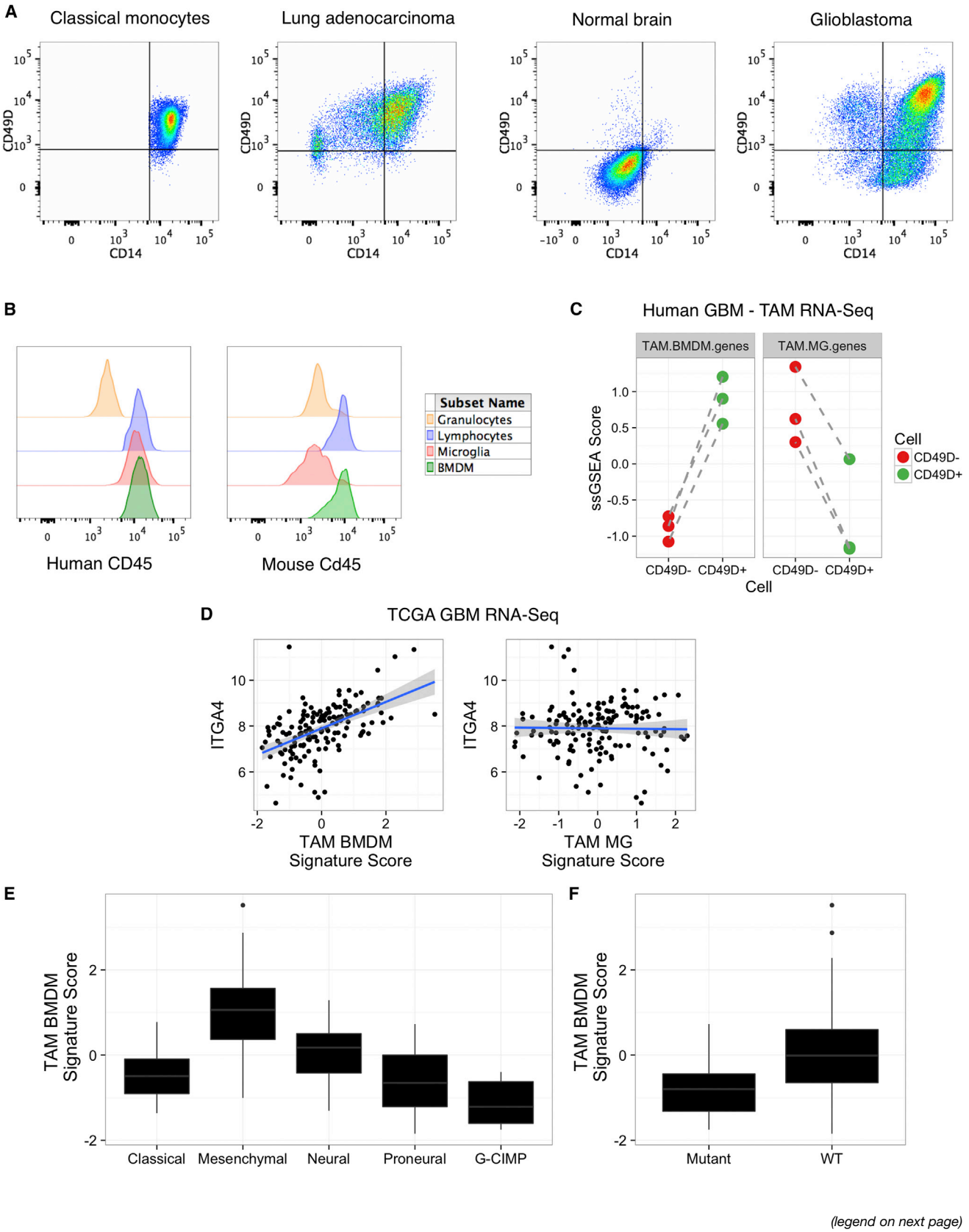

(legend on next page)

express CD49D, and were used as a reference guide for gating CD49D$^+$ and CD49D$^-$ TAMs (Figure S5A). Importantly, we never identified CD49D$^-$ TAMs in primary lung tumors or CD49D$^-$ monocytes in healthy donor PBMCs, indicating that, as predicted, low expression of CD49D is restricted to MG and is not a general phenotype of tissue-resident macrophages (Figure 5A). By contrast, the CD45$^+$CD11B$^+$CD66B$^-$CD14$^+$CD16$^-$ compartment in non-malignant brain was predominantly composed of CD49D$^-$ MG (Figure 5A). Critically, in each GBM sample we identified both CD49D$^+$ and CD49D$^-$ TAMs, presumably representing BMDM and brain-resident MG, respectively (Figure 5A).

Interestingly, in human samples, we found no difference in CD45 expression between CD49D$^-$ and CD49D$^+$ TAMs (Figure 5B), a marker previously suggested to be informative for distinguishing BMDMs and MG in brain malignancy (Hussain et al., 2006; Parney et al., 2009; Sedgwick et al., 1991). Indeed, CD45 expression differed most prominently between granulocytes and TAMs, as opposed to MG and BMDMs (Figure 5B). However, this lack of differential CD45 expression is not the case in mouse, where Cd45 adequately discriminates MG and BMDM in the models tested (Figure 5B). We next sorted paired CD49D$^-$ and CD49D$^+$ TAMs from GBM patients to verify these populations indeed reflected TAM MG and TAM BMDMs, respectively. Using genes specific for TAM MG and TAM BMDMs from our mouse models (Figure 2A), we found that CD49D$^-$ TAMs were indeed enriched for TAM MG genes ($p \leq 7.78 \times 10^{-3}$), while CD49D$^+$ TAMs were enriched for TAM BMDM genes ($p \leq 5.01 \times 10^{-3}$) (Figure 5C).

Previous analyses of TAM expression in human gliomas have utilized bulk CD11B$^+$ cells, a population likely composed of both TAM BMDMs and TAM MG, as well as other myeloid populations. We queried one available RNA-seq dataset from bulk CD11B$^+$ cells (Szulzewsky et al., 2016), which showed increased *ITGA4*/CD49D expression in purified CD11B$^+$ cells in GBM compared to normal MG from either post-mortem samples or resections from epileptic patients (Figure S5B). This was complemented by a relative decrease in the MG-enriched transcript *P2RY12* in GBM compared to non-malignant brain (Figure S5B). In querying an additional microarray-based dataset of purified CD11B$^+$ cells (Gabrusiewicz et al., 2016), we observed that peripheral blood CD11B$^+$ cells from GBM patients expressed similar levels of *ITGA4* compared to GBM tumor samples, while there was higher *P2RY12* expression in GBM samples than in peripheral blood (Figure S5C), as we would have expected. We extended these analyses to whole-tissue RNA-seq data from the TCGA-GBM cohort (Brennan et al., 2013) and observed that *ITGA4* expression was significantly increased in GBM compared to normal brain (Figure S5D). Collectively, these analyses suggest that TAMs in GBM represent a heterogeneous population composed of both BMDMs and MG, reinforcing the necessity of refined sorting strategies for accurate discrimination between these cells and highlighting the utility of a CD49D-based gating approach.

We next assessed TAM BMDM and TAM MG gene set expression in the TCGA cohort as a whole. TAM BMDM genes and TAM MG genes showed high intra-gene set correlation, where TAM BMDM genes such as *RUNX2*, *IL10*, *RUNX3*, *ITGA4*, and *VDR* showed significant pairwise correlations and TAM MG genes such as *MEF2C*, *P2RY12*, *RXRG*, *SALL1*, *KLF12* and *SALL3* similarly showed significant pairwise correlations (Figure S5E). Moreover, *ITGA4* showed a high correlation with a TAM BMDM gene signature score ($p \leq 2.2 \times 10^{-16}$), but not with a TAM MG signature score (Figure 5D), showing increased *ITGA4* expression is specific to TAM BMDM abundance and not TAMs as a whole.

Previous transcriptional and epigenetic analyses have identified distinct GBM subtypes (Noushmehr et al., 2010; Verhaak et al., 2010), where the mesenchymal subtype was enriched for tumor stroma and inflammatory molecules. Here, we find TAM BMDM signature scores are significantly different among molecular subtypes of GBM ($p \leq 2.2 \times 10^{-16}$), with the highest scores in the mesenchymal GBM subtype and the lowest scores in G-CIMP patients (Figure 5E). Correspondingly, TAM BMDM signature scores were lowest in patients with *IDH1* mutations (Figure 5F; $p \leq 5.93 \times 10^{-3}$). By comparison, TAM MG signature scores displayed a blunted association with tumor subtype ($p \leq 0.041$) and no association with *IDH1* mutation status ($p \leq 0.153$) (Figures S5F and S5G). These analyses reinforce our findings that TAM BMDMs and TAM MG are distinguishable immune cell populations with distinct abundance and characteristics in specific subtypes of human GBM.

DISCUSSION

IR-BMT has been used widely in animal models to perform lineage tracing of TAMs in brain malignancy (Ajami et al., 2007; De

Figure 5. CD49D Discriminates TAM BMDMs and TAM MG in Human Brain Malignancy

(A) Classical monocytes, MG, and TAMs were defined as CD45$^+$CD11B$^+$CD66B$^-$CD14$^+$CD16$^-$. Gated cells are then shown for CD14 and CD49D in representative samples of human classical monocytes from peripheral blood (n = 6), TAMs from a lung adenocarcinoma patient (n = 6), MG from a non-malignant brain (n = 3), and TAMs from a GBM patient (n = 3).

(B) Histogram of CD45 expression by flow cytometry in human (left) and mouse (right) samples. In human GBM, CD45 expression is shown for granulocytes (CD45$^+$CD11B$^+$CD66B$^+$CD16$^+$CD14^{low}), lymphocytes (CD45$^+$CD11B$^-$), TAM MG (CD45$^+$CD11B$^+$CD66B$^-$CD16$^-$CD14$^+$CD49D$^-$), and TAM BMDMs (CD45$^+$CD11B$^+$ CD66B$^-$CD16$^-$CD14$^+$CD49D$^+$). In mouse, Cd45 expression is shown for granulocytes (Cd45$^+$Cd11b$^+$Ly6C^{low}Ly6G$^+$), lymphocytes (Cd45$^+$Cd11b$^-$), TAM MG (Cd45$^+$Cd11b$^+$Ly6C$^-$Ly6G$^-$Tomato$^+$GFP$^-$), and TAM BMDMs (Cd45$^+$Cd11b$^+$Ly6C$^-$Ly6G$^-$Tomato$^-$GFP$^+$) from a Flt3:Cre Rosa26:mTmG GEMM-shP53 glioma. Data are representative of n = 3 patients and n = 5 mice.

(C) *Z* scored single sample gene set enrichment analysis (ssGSEA) scores for TAM BMDM genes (left, paired t test, $p \leq 5.01 \times 10^{-3}$) and TAM MG genes (right, paired t test, $p \leq 7.78 \times 10^{-3}$) in matched CD49D$^-$ and CD49D$^+$ TAMs from GBM patients. Dashed lines indicate matched samples (n = 3 patients).

(D) Scatterplot of TAM BMDM signature score (x axis, left, Spearman rho = 0.564, $p \leq 2.2 \times 10^{-16}$) and TAM MG signature score (x axis, right, Spearman rho = 0.067, $p \leq 0.411$) and *ITGA4* expression (y axis) from TCGA-GBM RNA-seq data. Solid blue line indicates line of best fit, with shaded areas depicting SD confidence intervals.

(E and F) *Z* scored TAM BMDM signature scores across (E) GBM subtype (ANOVA $p \leq 2.2 \times 10^{-16}$) and (F) *IDH1* mutation status (Student's t test $p \leq 5.93 \times 10^{-3}$).

Palma et al., 2005; Huang et al., 2014; Mildner et al., 2007; Müller et al., 2015), albeit with concerns regarding potential artifacts due to effects of IR on BBB disruption. Alternative chemical BMT approaches have been suggested, though similar effects on BBB permeability cannot be ignored (Alder et al., 2008; Kierdorf et al., 2013b). Here, we confirm that IR-BMT leads to increased TAM BMDM content in the GL261 glioma model, a finding that has been recently reported by juxtaposing IR-BMT with and without head-shielding (Müller et al., 2015). While IR-BMT may confound lineage-tracing studies, it remains to be seen if IR preconditioning before the onset of tumorigenesis significantly alters TAM activity in tumor development or if the inflammatory environment of the tumor supersedes any antecedent effects of the IR-BMT protocol.

Other than IR-BMT, the most widely employed approach to discriminate MG and peripherally derived macrophages relies upon Cd45 expression, with $Cd45^{high}$ cells considered BMDMs and $Cd45^{low}$ cells considered MG (Gabrusiewicz et al., 2011; Sedgwick et al., 1991). While this marker seems adequate in the murine models we have employed here, cell-type-specific CD45 expression appears to be different between mouse and human. Our data indicate that CD45 does not accurately discriminate MG and BMDMs in patient samples, emphasizing the need for extensive flow cytometry panels to clearly distinguish these cells in both species. Additionally, our genetic lineage tracing models also show that expression of *Cx3cr1*, which is commonly used to trace normal MG, is subject to upregulation in BMDMs upon tumor education (Figures 2A, S1F, and S4E) and thus cannot be used to discriminate MG and BMDMs in brain tumors.

Instead, we present *Itga4* (Cd49d) as an effective, consistent marker that works in both mice and humans to distinguish MG and peripherally derived macrophages in multiple brain malignancies. Cd49d may also prove a useful tool in determining the precise origin and kinetics of peripherally derived macrophages in brain tumors. Recent efforts to understand the heterogeneity and origins of non-parenchymal myeloid cells in the brain (including perivascular, meningeal, and choroid plexus macrophages) revealed that a subset of these cells are labeled using similar Flt3-Cre and Cx3cr1-CreER based lineage tracing systems as employed here (Goldmann et al., 2016). Thus it will be of interest to determine if any of these populations, in addition to monocytes, contribute to the TAM pool.

Our data support the hypothesis that epigenetic states influence stimulus-dependent transcriptional induction, thus leading to differential TAM education between MG and BMDMs. Differential genomic occupancy of PU.1 between MG and other macrophage populations in non-cancer contexts has been shown to dictate differential enhancer selection (Gosselin et al., 2014). Indeed, within this dataset, we found that PU.1 binding sites at enhancers and promoters were already different between MG and BMDM for the genes we identified to be specific to their respective TAM populations. This suggests that TAM BMDMs and TAM MG are poised to engage in different transcriptional networks based on initial enhancer selection. It is likely that differential expression of binding partners influences PU.1 genomic occupation. Cooperative binding is evident between PU.1 and CEBPβ to promote macrophage differentiation and in B cell development, where PU.1 occupancy is influenced by E2A expression (Heinz et al., 2010). Such a hypothesis has also been shown to account for MG-specific PU.1 binding in cooperation with TGF-β-induced SMAD activity (Gosselin et al., 2014). Similar dynamics may be at play in brain tumors, where binding partners that are absent in MG and expressed in BMDMs can sculpt genomic PU.1 occupancy. For example, the RUNX family member *Runx3* is one such candidate, which is enriched in TAM BMDMs versus TAM MG and shows motif enrichment in promoters where PU.1 binds in BMDMs, but not MG.

While our studies here focus predominantly on identifying recurrent signatures distinguishing TAM MG and TAM BMDMs across multiple mouse models and patient samples, there were also tumor-specific gene expression patterns in TAM education (Figures 2E, S2C, and S2D), which may provide insights into how tumor-derived signals can generate inter-tumoral heterogeneity in TAM activation profiles. In addition, analysis of TCGA data showed that gene signatures associated with TAM BMDMs were differentially enriched in the distinct tumor subtypes of GBM. Recent reports have identified mixed activation states in bulk TAM populations in glioma patients (Gabrusiewicz et al., 2016; Szulzewsky et al., 2016), and our data now show that TAM MG and TAM BMDMs possess distinct activation states, potentially resolving this mixed phenotype. Importantly, the identification of CD49D as a cell-surface marker to discriminate between TAM MG and TAM BMDMs in human disease will permit extensive interrogation of these cell populations in patient samples.

Collectively, the studies presented here definitively demonstrate that peripherally derived macrophages are indeed present in multiple mouse and human brain malignancies and have distinct transcriptional profiles from their brain-resident counterparts. We posit that while macrophages can acquire tissue-resident macrophage-like traits upon entry into a tissue (Lavin et al., 2014), an inflammatory microenvironment, such as in the context of cancer or neuroinflammation, may further amplify differences between the cells, leading to diverse functional outcomes for tissue-resident and peripherally derived macrophage populations.

EXPERIMENTAL PROCEDURES

Tumor and Lineage Tracing Models

Mouse models of gliomagenesis and brain metastasis, cell line generation, and the use of lineage tracing models have been previously reported (Boyer et al., 2011; Parkhurst et al., 2013; Quail et al., 2016; Sevenich et al., 2014) and are described in full in Supplemental Experimental Procedures.

Institutional Review Board Approval and Patient Information

All human specimens were collected from patients consented to Memorial Sloan Kettering Cancer Center (MSKCC) institutional review board (IRB) protocols #06-107, #14-230. Glioma patients that presented with contrast-enhancing brain lesions and no prior history of brain malignancy or therapy were included. Tumor specimens were collected from the operating room and processed as described below. Pathological analyses confirmed grade IV GBM. Non-malignant normal brain samples were collected from two sources: non-malignant sites distant from low-grade disease and post-mortem samples with no history of brain malignancy. Pathological analysis confirmed the absence of tumor. Samples from patients with primary lung tumors were

included based on pathological analysis of lung adenocarcinoma, with no screening based on prior malignancy or therapy.

Flow Cytometry and Cell Sorting

For blood analysis, mice were bled via either retro-orbital or submandibular routes under isoflurane anesthesia. For all other tissue analyses, mice were anesthetized with 1.25% avertin and transcardially perfused with PBS. Single-cell suspensions from spleen and bone marrow were isolated by macrodissection and mechanical tissue dissociation. Liver, kidney, and lung were macrodissected and dissociated using the Mouse Tumor Dissociation Kit (mTDK; Miltenyi) and the OctoMACS dissociator. Mouse and human brain specimens were macrodissected and dissociated using the Brain Tumor Dissociation Kit (BTDK; Miltenyi) and a single-cell suspension generated using the OctoMACS dissociator. Human lung tumors were dissociated with the Human Tumor Dissociation Kit (hTDK; Miltenyi.) All tissue suspensions were filtered through a 40-μM mesh filter and underwent red blood cell lysis (PharmLyse BD). Normal brain and brain tumor tissues were incubated with Myelin Removal Beads (Miltenyi). Single-cell suspensions were FC blocked (BD #553141) for 15 min at 4°C and then incubated with directly conjugated antibody panels for 15 min at 4°C. Cell suspensions were washed (PBS + 2% fetal bovine serum) and resuspended in a DAPI solution. All flow cytometry analysis was completed on a BD Fortessa device, and all sorting was performed on an Aria III. Cells were sorted directly into TRIzol LS and snap frozen in liquid nitrogen. Antibodies and methods for immunohistochemistry can be found in Supplemental Experimental Procedures.

Statistical Methods

RNA Sequencing, ATAC Sequencing, and Bioinformatics

RNA was isolated by chloroform extraction and isopropanol precipitation. RNA-sequencing libraries were generated with the SMART-Seq preparation kit (CloneTech). Single-end, 100-bp sequencing was performed by GeneWiz on an Illumina HiSeq 2500. FASTQ files were mapped to the mouse genome (mm10) or the human genome (hg19) using STAR (version 2.5.0e) with default parameters (Dobin et al., 2013). Transcript abundance was quantified using STAR with a GTF file from iGenomes (Illumina). A count matrix was produced in R and differential gene expression was assessed with DESeq2 using a fold change cutoff of ±2 and a false discovery rate of 5% (Love et al., 2014). Gene Ontology analysis was performed using DAVID with default parameters (Dennis et al., 2003). ATAC-sequencing was performed as previously described (Buenrostro et al., 2013). Paired-end, 50-bp sequencing was performed on an Illumina HiSeq 2500 with an average read depth of ~35,000,000 reads per sample. Reads were mapped to mm10 using STAR (version 2.5.0e) using (–alignIntronMax 1–alignEndsType EndToEnd). Peak calling, annotation, and differential peak identification was performed using HOMER.

Methods for analyzing external datasets, TF activity analysis, and additional statistical methods are described in Supplemental Experimental Procedures.

ACCESSION NUMBERS

The accession number for the gene expression and ATAC-sequencing data generated in this study is GEO: GSE86573.

SUPPLEMENTAL INFORMATION

Supplemental Information includes Supplemental Experimental Procedures, five figures, and five tables and can be found with this article online at http://dx.doi.org/10.1016/j.celrep.2016.10.052.

AUTHOR CONTRIBUTIONS

R.L.B. and J.A.J. conceived the study, designed and interpreted experiments, and wrote the manuscript. R.L.B., F.K., L.A., S.M.P., L.S., D.F.Q., S.D., and K.S. performed experiments and analyzed results. R.L.B. performed all computational analyses. E.E.G., C.A.I.-D., C.W.B., V.T., and P.H.G. provided patient samples. J.A.J. supervised the study. All authors commented on the manuscript.

ACKNOWLEDGMENTS

We thank X. Chen for excellent technical support, Drs. D. Yan and N. Ben-Chetrit for experimental assistance, and members of the J.A.J. lab for insightful comments and discussion. We are grateful to Dr. B. Santomasso, N. Distefano, and Dr. L. DeAngelis (MSKCC Neurosurgery) and Dr. C. Rudin (MSKCC Thoracic Oncology) for help in acquiring patient samples. We thank Drs. E. Holland and T. Ozawa for generously providing the RCAS vectors and Nestin-Tva mice, Dr. C. Forsberg for the *Flt3:Cre Rosa26:mTmG* mice, Drs. C. Sawyers and B. Carver for the *Pten*$^{Flox/Flox}$ mice, Drs. S. Coniglio and J. Segall for the GL261 cell line, and Dr. J. Massagué for the brain-homing MDA-MB-231 cell line. This research was supported by grant R01CA181355 (J.A.J.), the Ludwig Institute for Cancer Research (J.A.J.), the MSKCC Center for Metastasis Research (J.A.J.), MSK Cancer Center Support grant P30 CA008748 from the National Cancer Institute, the Gerstner Sloan Kettering Graduate School (R.L.B.), National Cancer Institute fellowship 5F31CA167863 (R.L.B.), Deutsche Forschungsgemeinschaft fellowships KL 2491/1-1 (F.K.) and SE2234/1-1 (L.S.), the American Brain Tumor Association in honor of Joel A. Gingras (L.A.), and the Canadian Institutes of Health Research (D.F.Q.).

Received: September 18, 2016
Revised: October 12, 2016
Accepted: October 19, 2016
Published: November 10, 2016

REFERENCES

Ajami, B., Bennett, J.L., Krieger, C., Tetzlaff, W., and Rossi, F.M. (2007). Local self-renewal can sustain CNS microglia maintenance and function throughout adult life. Nat. Neurosci. *10*, 1538–1543.

Alder, J.K., Georgantas, R.W., 3rd, Hildreth, R.L., Kaplan, I.M., Morisot, S., Yu, X., McDevitt, M., and Civin, C.I. (2008). Kruppel-like factor 4 is essential for inflammatory monocyte differentiation in vivo. J. Immunol. *180*, 5645–5652.

Biffi, A., De Palma, M., Quattrini, A., Del Carro, U., Amadio, S., Visigalli, I., Sessa, M., Fasano, S., Brambilla, R., Marchesini, S., et al. (2004). Correction of metachromatic leukodystrophy in the mouse model by transplantation of genetically modified hematopoietic stem cells. J. Clin. Invest. *113*, 1118–1129.

Bos, P.D., Zhang, X.H., Nadal, C., Shu, W., Gomis, R.R., Nguyen, D.X., Minn, A.J., van de Vijver, M.J., Gerald, W.L., Foekens, J.A., and Massagué, J. (2009). Genes that mediate breast cancer metastasis to the brain. Nature *459*, 1005–1009.

Boyer, S.W., Schroeder, A.V., Smith-Berdan, S., and Forsberg, E.C. (2011). All hematopoietic cells develop from hematopoietic stem cells through Flk2/Flt3-positive progenitor cells. Cell Stem Cell *9*, 64–73.

Brennan, C.W., Verhaak, R.G., McKenna, A., Campos, B., Noushmehr, H., Salama, S.R., Zheng, S., Chakravarty, D., Sanborn, J.Z., Berman, S.H., et al.; TCGA Research Network (2013). The somatic genomic landscape of glioblastoma. Cell *155*, 462–477.

Bruttger, J., Karram, K., Wörtge, S., Regen, T., Marini, F., Hoppmann, N., Klein, M., Blank, T., Yona, S., Wolf, Y., et al. (2015). Genetic cell ablation reveals clusters of local self-renewing microglia in the mammalian central nervous system. Immunity *43*, 92–106.

Buenrostro, J.D., Giresi, P.G., Zaba, L.C., Chang, H.Y., and Greenleaf, W.J. (2013). Transposition of native chromatin for fast and sensitive epigenomic profiling of open chromatin, DNA-binding proteins and nucleosome position. Nat. Methods *10*, 1213–1218.

Chopin, M., Seillet, C., Chevrier, S., Wu, L., Wang, H., Morse, H.C., 3rd, Belz, G.T., and Nutt, S.L. (2013). Langerhans cells are generated by two distinct PU.1-dependent transcriptional networks. J. Exp. Med. *210*, 2967–2980.

De Palma, M., Venneri, M.A., Galli, R., Sergi Sergi, L., Politi, L.S., Sampaolesi, M., and Naldini, L. (2005). Tie2 identifies a hematopoietic lineage of proangiogenic monocytes required for tumor vessel formation and a mesenchymal population of pericyte progenitors. Cancer Cell *8*, 211–226.

Dennis, G., Jr., Sherman, B.T., Hosack, D.A., Yang, J., Gao, W., Lane, H.C., and Lempicki, R.A. (2003). DAVID: Database for annotation, visualization, and integrated discovery. Genome Biol. *4*, 3.

Dobin, A., Davis, C.A., Schlesinger, F., Drenkow, J., Zaleski, C., Jha, S., Batut, P., Chaisson, M., and Gingeras, T.R. (2013). STAR: ultrafast universal RNA-seq aligner. Bioinformatics *29*, 15–21.

Domínguez-Soto, A., Relloso, M., Vega, M.A., Corbí, A.L., and Puig-Kröger, A. (2005). RUNX3 regulates the activity of the CD11a and CD49d integrin gene promoters. Immunobiology *210*, 133–139.

Du, R., Lu, K.V., Petritsch, C., Liu, P., Ganss, R., Passegué, E., Song, H., Vandenberg, S., Johnson, R.S., Werb, Z., and Bergers, G. (2008). HIF1alpha induces the recruitment of bone marrow-derived vascular modulatory cells to regulate tumor angiogenesis and invasion. Cancer Cell *13*, 206–220.

Dubois, L.G., Campanati, L., Righy, C., D'Andrea-Meira, I., Spohr, T.C., Porto-Carreiro, I., Pereira, C.M., Balça-Silva, J., Kahn, S.A., DosSantos, M.F., et al. (2014). Gliomas and the vascular fragility of the blood brain barrier. Front. Cell. Neurosci. *8*, 418.

Gabrusiewicz, K., Ellert-Miklaszewska, A., Lipko, M., Sielska, M., Frankowska, M., and Kaminska, B. (2011). Characteristics of the alternative phenotype of microglia/macrophages and its modulation in experimental gliomas. PLoS ONE *6*, e23902.

Gabrusiewicz, K., Rodriguez, B., Wei, J., Hashimoto, Y., Healy, L.M., Maiti, S.N., Thomas, G., Zhou, S., Wang, Q., Elakkad, A., et al. (2016). Glioblastoma-infiltrated innate immune cells resemble M0 macrophage phenotype. JCI Insight *1*, e85841.

Gautier, E.L., Shay, T., Miller, J., Greter, M., Jakubzick, C., Ivanov, S., Helft, J., Chow, A., Elpek, K.G., Gordonov, S., et al.; Immunological Genome Consortium (2012). Gene-expression profiles and transcriptional regulatory pathways that underlie the identity and diversity of mouse tissue macrophages. Nat. Immunol. *13*, 1118–1128.

Ginhoux, F., Greter, M., Leboeuf, M., Nandi, S., See, P., Gokhan, S., Mehler, M.F., Conway, S.J., Ng, L.G., Stanley, E.R., et al. (2010). Fate mapping analysis reveals that adult microglia derive from primitive macrophages. Science *330*, 841–845.

Goldmann, T., Wieghofer, P., Jordão, M.J., Prutek, F., Hagemeyer, N., Frenzel, K., Amann, L., Staszewski, O., Kierdorf, K., Krueger, M., et al. (2016). Origin, fate and dynamics of macrophages at central nervous system interfaces. Nat. Immunol. *17*, 797–805.

Gomez Perdiguero, E., Klapproth, K., Schulz, C., Busch, K., Azzoni, E., Crozet, L., Garner, H., Trouillet, C., de Bruijn, M.F., Geissmann, F., and Rodewald, H.R. (2015). Tissue-resident macrophages originate from yolk-sac-derived erythro-myeloid progenitors. Nature *518*, 547–551.

Gosselin, D., Link, V.M., Romanoski, C.E., Fonseca, G.J., Eichenfield, D.Z., Spann, N.J., Stender, J.D., Chun, H.B., Garner, H., Geissmann, F., and Glass, C.K. (2014). Environment drives selection and function of enhancers controlling tissue-specific macrophage identities. Cell *159*, 1327–1340.

Heinz, S., Benner, C., Spann, N., Bertolino, E., Lin, Y.C., Laslo, P., Cheng, J.X., Murre, C., Singh, H., and Glass, C.K. (2010). Simple combinations of lineage-determining transcription factors prime cis-regulatory elements required for macrophage and B cell identities. Mol. Cell *38*, 576–589.

Huang, Y., Hoffman, C., Rajappa, P., Kim, J.H., Hu, W., Huse, J., Tang, Z., Li, X., Weksler, B., Bromberg, J., et al. (2014). Oligodendrocyte progenitor cells promote neovascularization in glioma by disrupting the blood-brain barrier. Cancer Res. *74*, 1011–1021.

Huse, J.T., Brennan, C., Hambardzumyan, D., Wee, B., Pena, J., Rouhanifard, S.H., Sohn-Lee, C., le Sage, C., Agami, R., Tuschl, T., and Holland, E.C. (2009). The PTEN-regulating microRNA miR-26a is amplified in high-grade glioma and facilitates gliomagenesis in vivo. Genes Dev. *23*, 1327–1337.

Hussain, S.F., Yang, D., Suki, D., Aldape, K., Grimm, E., and Heimberger, A.B. (2006). The role of human glioma-infiltrating microglia/macrophages in mediating antitumor immune responses. Neuro-oncol. *8*, 261–279.

Kennedy, D.W., and Abkowitz, J.L. (1997). Kinetics of central nervous system microglial and macrophage engraftment: analysis using a transgenic bone marrow transplantation model. Blood *90*, 986–993.

Kierdorf, K., Erny, D., Goldmann, T., Sander, V., Schulz, C., Perdiguero, E.G., Wieghofer, P., Heinrich, A., Riemke, P., Hölscher, C., et al. (2013a). Microglia emerge from erythromyeloid precursors via Pu.1- and Irf8-dependent pathways. Nat. Neurosci. *16*, 273–280.

Kierdorf, K., Katzmarski, N., Haas, C.A., and Prinz, M. (2013b). Bone marrow cell recruitment to the brain in the absence of irradiation or parabiosis bias. PLoS ONE *8*, e58544.

Lavin, Y., Winter, D., Blecher-Gonen, R., David, E., Keren-Shaul, H., Merad, M., Jung, S., and Amit, I. (2014). Tissue-resident macrophage enhancer landscapes are shaped by the local microenvironment. Cell *159*, 1312–1326.

Liu, W.Y., Wang, Z.B., Zhang, L.C., Wei, X., and Li, L. (2012). Tight junction in blood-brain barrier: an overview of structure, regulation, and regulator substances. CNS Neurosci. Ther. *18*, 609–615.

Locatelli, G., Wörtge, S., Buch, T., Ingold, B., Frommer, F., Sobottka, B., Krüger, M., Karram, K., Bühlmann, C., Bechmann, I., et al. (2012). Primary oligodendrocyte death does not elicit anti-CNS immunity. Nat. Neurosci. *15*, 543–550.

Love, M.I., Huber, W., and Anders, S. (2014). Moderated estimation of fold change and dispersion for RNA-seq data with DESeq2. Genome Biol. *15*, 550.

Mass, E., Ballesteros, I., Farlik, M., Halbritter, F., Günther, P., Crozet, L., Jacome-Galarza, C.E., Händler, K., Klughammer, J., Kobayashi, Y., et al. (2016). Specification of tissue-resident macrophages during organogenesis. Science *353*, aaf4238.

Mildner, A., Schmidt, H., Nitsche, M., Merkler, D., Hanisch, U.K., Mack, M., Heikenwalder, M., Brück, W., Priller, J., and Prinz, M. (2007). Microglia in the adult brain arise from Ly-6ChiCCR2+ monocytes only under defined host conditions. Nat. Neurosci. *10*, 1544–1553.

Mosser, D.M., and Edwards, J.P. (2008). Exploring the full spectrum of macrophage activation. Nat. Rev. Immunol. *8*, 958–969.

Müller, A., Brandenburg, S., Turkowski, K., Müller, S., and Vajkoczy, P. (2015). Resident microglia, and not peripheral macrophages, are the main source of brain tumor mononuclear cells. Int. J. Cancer *137*, 278–288.

Murray, P.J., Allen, J.E., Biswas, S.K., Fisher, E.A., Gilroy, D.W., Goerdt, S., Gordon, S., Hamilton, J.A., Ivashkiv, L.B., Lawrence, T., et al. (2014). Macrophage activation and polarization: nomenclature and experimental guidelines. Immunity *41*, 14–20.

Noushmehr, H., Weisenberger, D.J., Diefes, K., Phillips, H.S., Pujara, K., Berman, B.P., Pan, F., Pelloski, C.E., Sulman, E.P., Bhat, K.P., et al.; Cancer Genome Atlas Research Network (2010). Identification of a CpG island methylator phenotype that defines a distinct subgroup of glioma. Cancer Cell *17*, 510–522.

Okabe, Y., and Medzhitov, R. (2016). Tissue biology perspective on macrophages. Nat. Immunol. *17*, 9–17.

Opitz, C.A., Litzenburger, U.M., Sahm, F., Ott, M., Tritschler, I., Trump, S., Schumacher, T., Jestaedt, L., Schrenk, D., Weller, M., et al. (2011). An endogenous tumour-promoting ligand of the human aryl hydrocarbon receptor. Nature *478*, 197–203.

Ostuni, R., and Natoli, G. (2011). Transcriptional control of macrophage diversity and specialization. Eur. J. Immunol. *41*, 2486–2490.

Ozawa, T., Riester, M., Cheng, Y.K., Huse, J.T., Squatrito, M., Helmy, K., Charles, N., Michor, F., and Holland, E.C. (2014). Most human non-GCIMP glioblastoma subtypes evolve from a common proneural-like precursor glioma. Cancer Cell *26*, 288–300.

Parkhurst, C.N., Yang, G., Ninan, I., Savas, J.N., Yates, J.R., 3rd, Lafaille, J.J., Hempstead, B.L., Littman, D.R., and Gan, W.B. (2013). Microglia promote learning-dependent synapse formation through brain-derived neurotrophic factor. Cell *155*, 1596–1609.

Parney, I.F., Waldron, J.S., and Parsa, A.T. (2009). Flow cytometry and in vitro analysis of human glioma-associated macrophages. Laboratory investigation. J. Neurosurg. *110*, 572–582.

Pyonteck, S.M., Akkari, L., Schuhmacher, A.J., Bowman, R.L., Sevenich, L., Quail, D.F., Olson, O.C., Quick, M.L., Huse, J.T., Teijeiro, V., et al. (2013). CSF-1R inhibition alters macrophage polarization and blocks glioma progression. Nat. Med. *19*, 1264–1272.

Quail, D.F., Bowman, R.L., Akkari, L., Quick, M.L., Schuhmacher, A.J., Huse, J.T., Holland, E.C., Sutton, J.C., and Joyce, J.A. (2016). The tumor microenvironment underlies acquired resistance to CSF-1R inhibition in gliomas. Science *352*, aad3018.

Reith, W., LeibundGut-Landmann, S., and Waldburger, J.M. (2005). Regulation of MHC class II gene expression by the class II transactivator. Nat. Rev. Immunol. *5*, 793–806.

Schulz, C., Gomez Perdiguero, E., Chorro, L., Szabo-Rogers, H., Cagnard, N., Kierdorf, K., Prinz, M., Wu, B., Jacobsen, S.E., Pollard, J.W., et al. (2012). A lineage of myeloid cells independent of Myb and hematopoietic stem cells. Science *336*, 86–90.

Sedgwick, J.D., Schwender, S., Imrich, H., Dörries, R., Butcher, G.W., and ter Meulen, V. (1991). Isolation and direct characterization of resident microglial cells from the normal and inflamed central nervous system. Proc. Natl. Acad. Sci. USA *88*, 7438–7442.

Sevenich, L., Bowman, R.L., Mason, S.D., Quail, D.F., Rapaport, F., Elie, B.T., Brogi, E., Brastianos, P.K., Hahn, W.C., Holsinger, L.J., et al. (2014). Analysis of tumour- and stroma-supplied proteolytic networks reveals a brain-metastasis-promoting role for cathepsin S. Nat. Cell Biol. *16*, 876–888.

Solga, A.C., Pong, W.W., Kim, K.Y., Cimino, P.J., Toonen, J.A., Walker, J., Wylie, T., Magrini, V., Griffith, M., Griffith, O.L., et al. (2015). RNA sequencing of tumor-associated microglia reveals Ccl5 as a stromal chemokine critical for Neurofibromatosis-1 glioma growth. Neoplasia *17*, 776–788.

Stephan, A.H., Barres, B.A., and Stevens, B. (2012). The complement system: an unexpected role in synaptic pruning during development and disease. Annu. Rev. Neurosci. *35*, 369–389.

Szulzewsky, F., Arora, S., de Witte, L., Ulas, T., Markovic, D., Schultze, J.L., Holland, E.C., Synowitz, M., Wolf, S.A., and Kettenmann, H. (2016). Human glioblastoma-associated microglia/monocytes express a distinct RNA profile compared to human control and murine samples. Glia *64*, 1416–1436.

Verhaak, R.G., Hoadley, K.A., Purdom, E., Wang, V., Qi, Y., Wilkerson, M.D., Miller, C.R., Ding, L., Golub, T., Mesirov, J.P., et al.; Cancer Genome Atlas Research Network (2010). Integrated genomic analysis identifies clinically relevant subtypes of glioblastoma characterized by abnormalities in PDGFRA, IDH1, EGFR, and NF1. Cancer Cell *17*, 98–110.

Villagra, A., Cheng, F., Wang, H.W., Suarez, I., Glozak, M., Maurin, M., Nguyen, D., Wright, K.L., Atadja, P.W., Bhalla, K., et al. (2009). The histone deacetylase HDAC11 regulates the expression of interleukin 10 and immune tolerance. Nat. Immunol. *10*, 92–100.

Xue, J., Schmidt, S.V., Sander, J., Draffehn, A., Krebs, W., Quester, I., De Nardo, D., Gohel, T.D., Emde, M., Schmidleithner, L., et al. (2014). Transcriptome-based network analysis reveals a spectrum model of human macrophage activation. Immunity *40*, 274–288.

Cell Reports, Volume *17*

Supplemental Information

Macrophage Ontogeny Underlies Differences in Tumor-Specific Education in Brain Malignancies

Robert L. Bowman, Florian Klemm, Leila Akkari, Stephanie M. Pyonteck, Lisa Sevenich, Daniela F. Quail, Surajit Dhara, Kenishana Simpson, Eric E. Gardner, Christine A. Iacobuzio-Donahue, Cameron W. Brennan, Viviane Tabar, Philip H. Gutin, and Johanna A. Joyce

Macrophage ontogeny underlies differences in tumor-specific education in brain malignancies

Robert L. Bowman[1,2], Florian Klemm[1,3,4], Leila Akkari[1,3,4], Stephanie M. Pyonteck[1], Lisa Sevenich[1], Daniela F. Quail[1], Surajit Dhara[5], Kenishana Simpson[1], Eric E. Gardner[6], Christine A. Iacobuzio-Donahue[5,7], Cameron W. Brennan[8], Viviane Tabar[8], Philip H. Gutin[8], and Johanna A. Joyce[1,3,4,#]

[#] Correspondence to: johanna@joycelab.org

Supplemental Figure 1: Genetic lineage tracing models provide high fidelity approaches for isolating TAM BMDM and TAM MG. Related to Figure 1.

Supplemental Figure 2: TAM BMDM and TAM MG possess model and cell type specific gene expression patterns associated with baseline chromatin states. Related to Figure 2.

Supplemental Figure 3: TAM BMDM and TAM MG possess differential open chromatin in cell-type specific genes. Related to Figure 3.

Supplemental Figure 4: Cd49d and Cd11a are enriched in TAM BMDM compared to TAM MG in multiple mouse models of brain malignancy. Related to Figure 4.

Supplemental Figure 5: *ITGA4* and markers of TAM BMDM are present in purified cell types and in whole tumor expression data from patients. Related to Figure 5.

SUPPLEMENTAL TABLES

Supplemental Table S1A and S1B: Conserved and specific genes upregulated in TAM populations compared to normal microglia and monocytes. Related to Figure 1I.

Supplemental Table S2: Differentially expressed genes between TAM BMDM and TAM MG in both GEMM and GL261 models. Related to Figure 2A.

Supplemental Table S3: Differentially expressed genes between GEMM and GL261 models for both TAM BMDM and TAM MG. Related to Figure 2A and Figure S2C.

Supplemental Table S4: Lists of cell type-specific and TAM education-specific gene sets for TAM BMDM and TAM MG. Related to Figure 2E and Figure S2D.

Supplemental Table S5A, S5B and S5C: Differentially enriched ATAC-Seq peaks, motif scores, and transcription factor activities between TAM BMDM and TAM MG. Related to Figure 3.

SUPPLEMENTAL EXPERIMENTAL PROCEDURES

Bowman et al, Figure S1

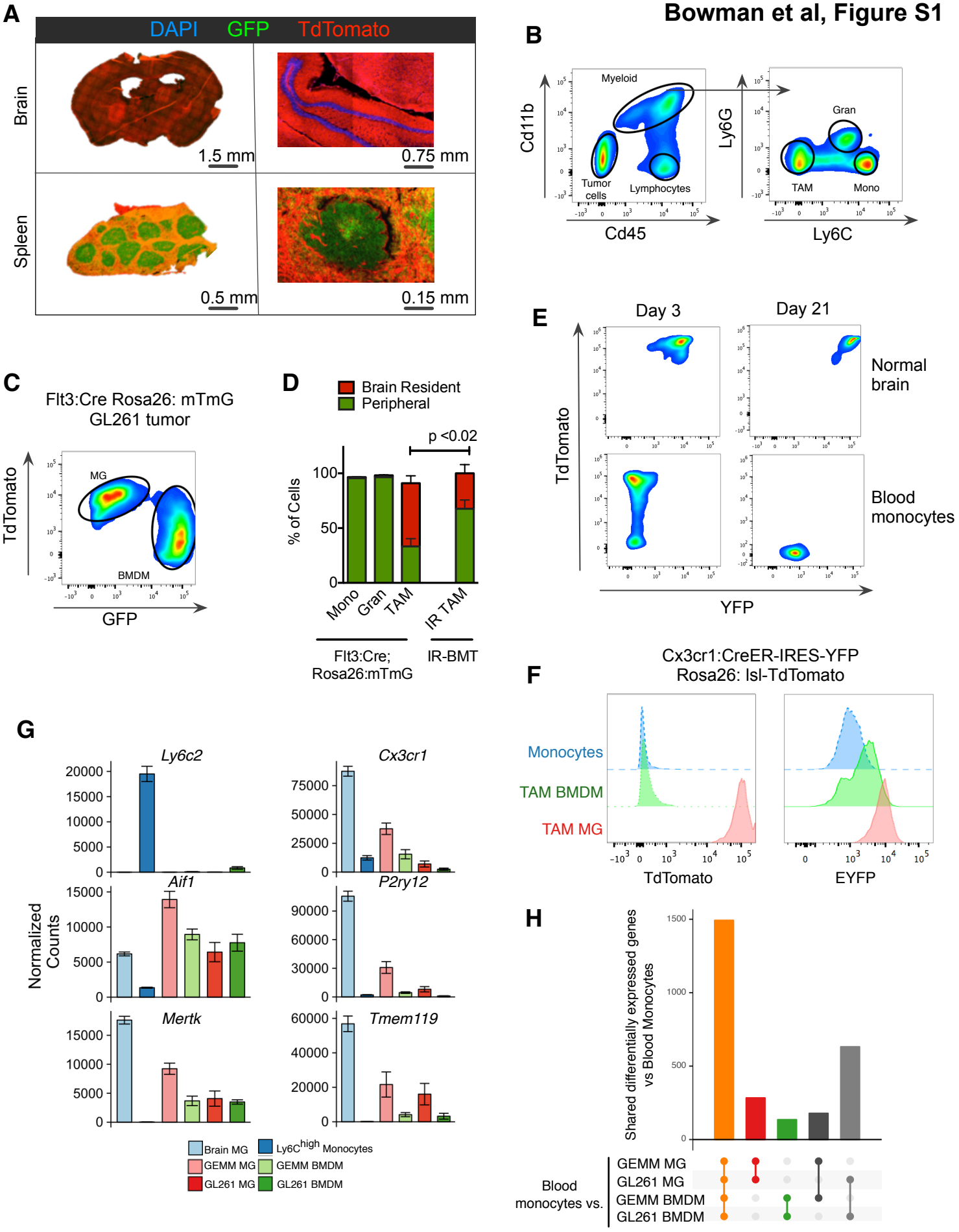

Supplemental Figure 1: Genetic lineage tracing models provide high fidelity approaches for isolating TAM BMDM and TAM MG. Related to Figure 1.

(A) Representative tiled immunofluorescence image of brain (top) and spleen (bottom) in a Flt:Cre Rosa26:mTmG mouse. TdTomato is indicated in red, GFP in green, and DAPI in blue. Scale bars are indicated on individual panels. Representative of n=3 mice. **(B)** Representative gating strategy from a Flt3:Cre, Rosa26:mTmG GEMM-shP53 tumor depicting TAM, granulocyte (Gran) and monocyte (Mono) identification in brain tumors. Bulk myeloid cells were first identified as $Cd45^{+}Cd11b^{+}$ and further subdivided into $Ly6C^{-}Ly6G^{-}$ TAM, $Ly6C^{low}Ly6G^{+}$ granulocytes, or $Ly6C^{+}Ly6G^{-}$ monocytes. **(C)** TAMs, as described in (B), from a Flt3:Cre Rosa26:mTmG GL261 tumor depicting both $TdTomato^{+}GFP^{-}$ microglia and $TdTomato^{-}GFP^{+}$ BMDM. Representative of n=3 mice. **(D)** Quantitation of $TdTomato^{+}$ and GFP^{+} monocytes, granulocytes and TAMs in GL261 tumors as depicted in (B,C) (left) or donor-GFP^{+} vs host-GFP^{-} TAMs from GL261 tumors in an irradiation-bone marrow transplantation lineage tracing model (right). Student's t-test $p \leq 0.02$. Bars represent mean and s.e.m. n=3-5 for each group. **(E)** Flow plots of TdTomato and eYFP expression in normal microglia (top) and blood monocytes (bottom) either 3 days (left) or 21 days (right) following tamoxifen treatment. Representative of n=4 mice. **(F)** Histogram of TdTomato (left) and eYFP (right) expression in tumor monocytes, TAM BMDM or TAM MG in the Cx3cr1:CreER-IRES-YFP; Rosa26:lslTdTomato; GL261 tumor model. Representative of n=6 mice. **(G)** Barplots of normalized RNA-seq counts for the *Ly6c2, Aif1, Mertk, Cx3cr1, P2ry12,* and *Tmem119* genes in the indicated cell populations. Bars represent mean ± s.e.m. **(H)** Differentially expressed genes between monocytes and the four TAM populations were identified (log2 fold change > ±1 and FDR<1%). Barchart depicts the number of differentially expressed genes that are shared between the different groups as in Figure 1I.

Bowman et al, Figure S2

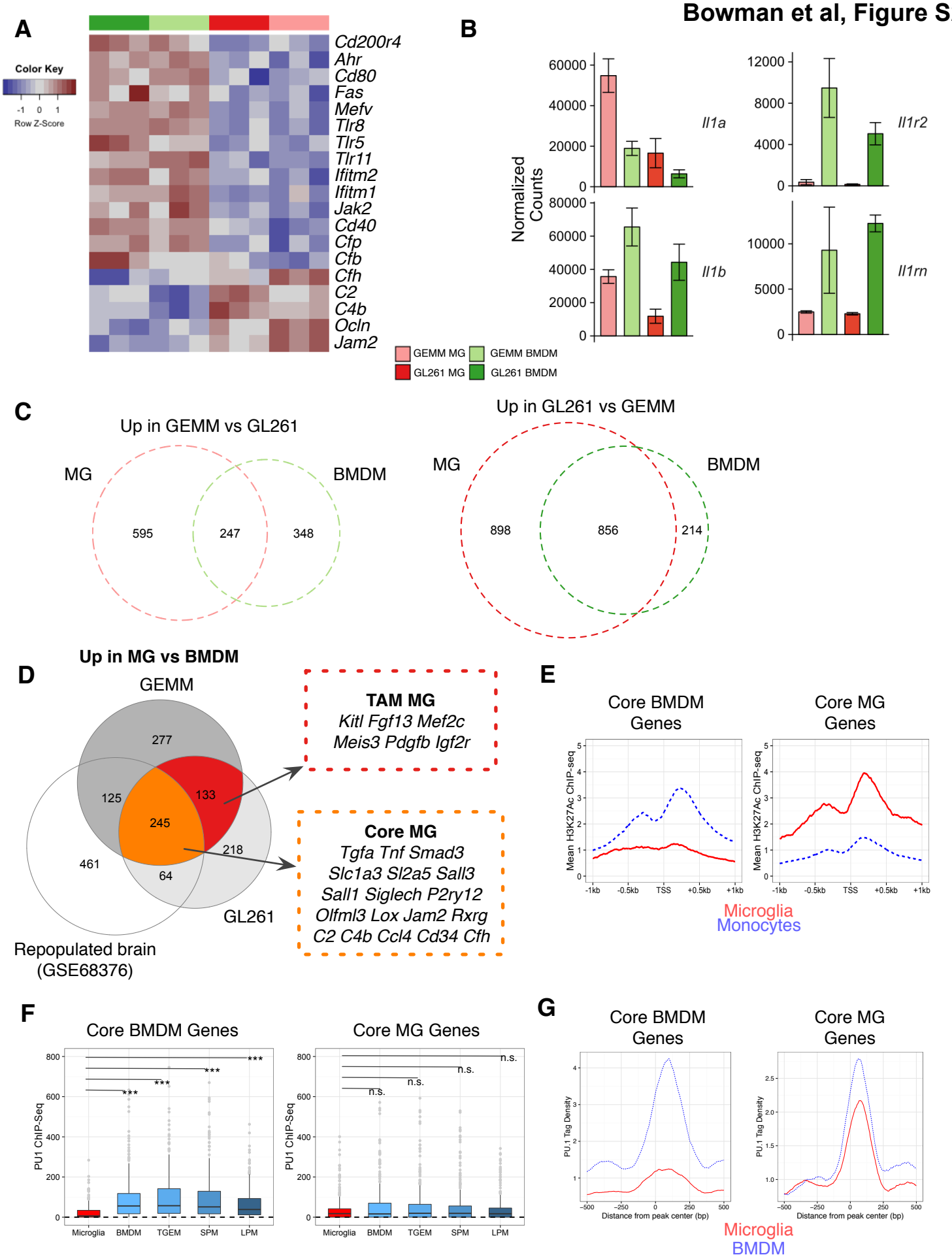

Supplemental Figure 2: TAM BMDM and TAM MG possess model and cell type specific gene expression patterns associated with baseline chromatin states. Related to Figure 2.

(A) Heatmap of row normalized gene expression values for the indicated genes across TAM BMDM and TAM MG from the GL261 and GEMM-shP53 models. **(B)** Barplots of normalized RNA-seq counts for *Il1a*, *Il1b*, *Il1r2* and *Il1rn.* Bars represent mean ± s.e.m. **(C)** Venn diagram of genes upregulated in TAM MG or TAM BMDM or both in the GEMM-shP53 model compared to the GL261 model (left). The right panel references genes that are upregulated in the GL261 model compared to the GEMM-shP53 model. **(D)** Venn diagram depicting significantly upregulated genes in MG vs BMDM in the GEMM-shP53 model, GL261 model, and non-malignant brain (GSE68376 dataset). The red sector (TAM MG genes) indicates genes that are enriched in TAM MG in both GEMM-shP53 and GL261 tumors, but are not differentially expressed in non-malignant brain. The orange sector (Core MG genes) highlights genes that are enriched in all three datasets. Select genes are listed. **(E)** Mean H3K27-Acetylation signal centered around the transcription start site (+/- 1 kb) in Core BMDM genes (left) and Core MG genes (right). Monocytes are shown in blue and microglia are shown in red. Data was downloaded and analyzed from GEO accession number GSE63339. **(F)** PU.1 binding intensity at the promoters of microglia, BMDM, thyoglycolate elicited peritoneal macrophages (TGEM), small peritoneal macrophages (SPM), and large peritoneal macrophages (LPM) for Core BMDM and Core MG genes. Genes were subset for those that showed binding of PU.1 in at least one of the macrophage populations. For Core BMDM genes with microglia vs BMDM $p \leq 7.6 \times 10^{-16}$; vs TGEM $p \leq 7.4 \times 10^{-29}$; vs SPM $p \leq 4.3 \times 10^{-29}$; vs LPM $p \leq 3.4 \times 10^{-14}$. **(G)** Mean PU.1 binding distribution in enhancers of Core BMDM and Core MG genes for microglia (red) and BMDM (blue). Enhancers were defined +/- 50 kb from the transcription start site (excluding the promoter). Data for (F) and (G) was downloaded and analyzed from GEO accession number GSE62826. n.s. denotes $p > 0.05$, *** denotes $p \leq 1 \times 10^{-13}$ evaluated with paired Student's t-test.

Bowman et al, Figure S3

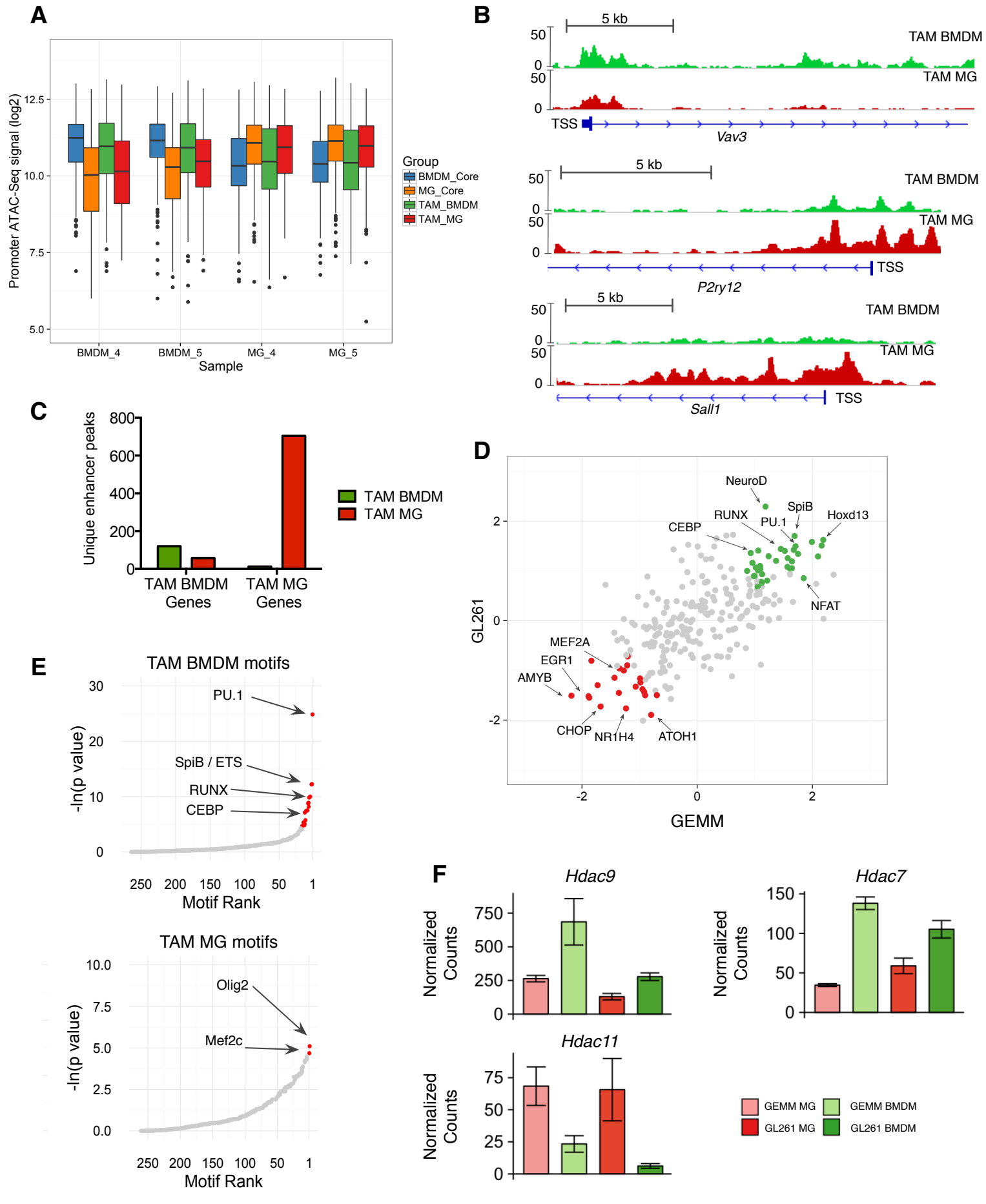

Supplemental Figure 3: TAM BMDM and TAM MG possess differential open chromatin in cell-type specific genes. Related to Figure 3.

(A) Boxplots for two matched TAM BMDM and TAM MG biological replicates of tag normalized log2 ATAC-Seq signal in the promoters of genes from the indicated gene sets, where each data point represents a score from a single promoter. **(B)** ATAC-Seq signal tracks for TAM BMDM (top, green) and TAM MG (bottom, red) around the transcription start site of *Vav3, P2ry12,* and *Sall1*. Y-axis value indicate tags per 10,000,000 with a range of 0-50. TSS denotes transcription start site. **(C)** Barplot depicting number of ATAC-seq peaks significantly enriched in either TAM BMDM or TAM MG in the indicated gene sets. **(D)** Scatterplot depicting differential transcription factor activity values between TAM BMDM and TAM MG in the GEMM-shP53 model (x-axis) and GL261 model (y-axis). Color scale and size of dot indicates relative enrichment for BMDM or MG specificity with green showing BMDM specificity and red showing MG specificity. **(E)** Ranked motifs based on –ln(p value) from HOMER for enrichment in either TAM BMDM (top) or TAM MG (bottom) genes. **(F)** Barplot depicting normalized gene counts of *Hdac7, Hdac9,* and *Hdac11* in the indicated TAM populations. Bars represent mean ± s.e.m.

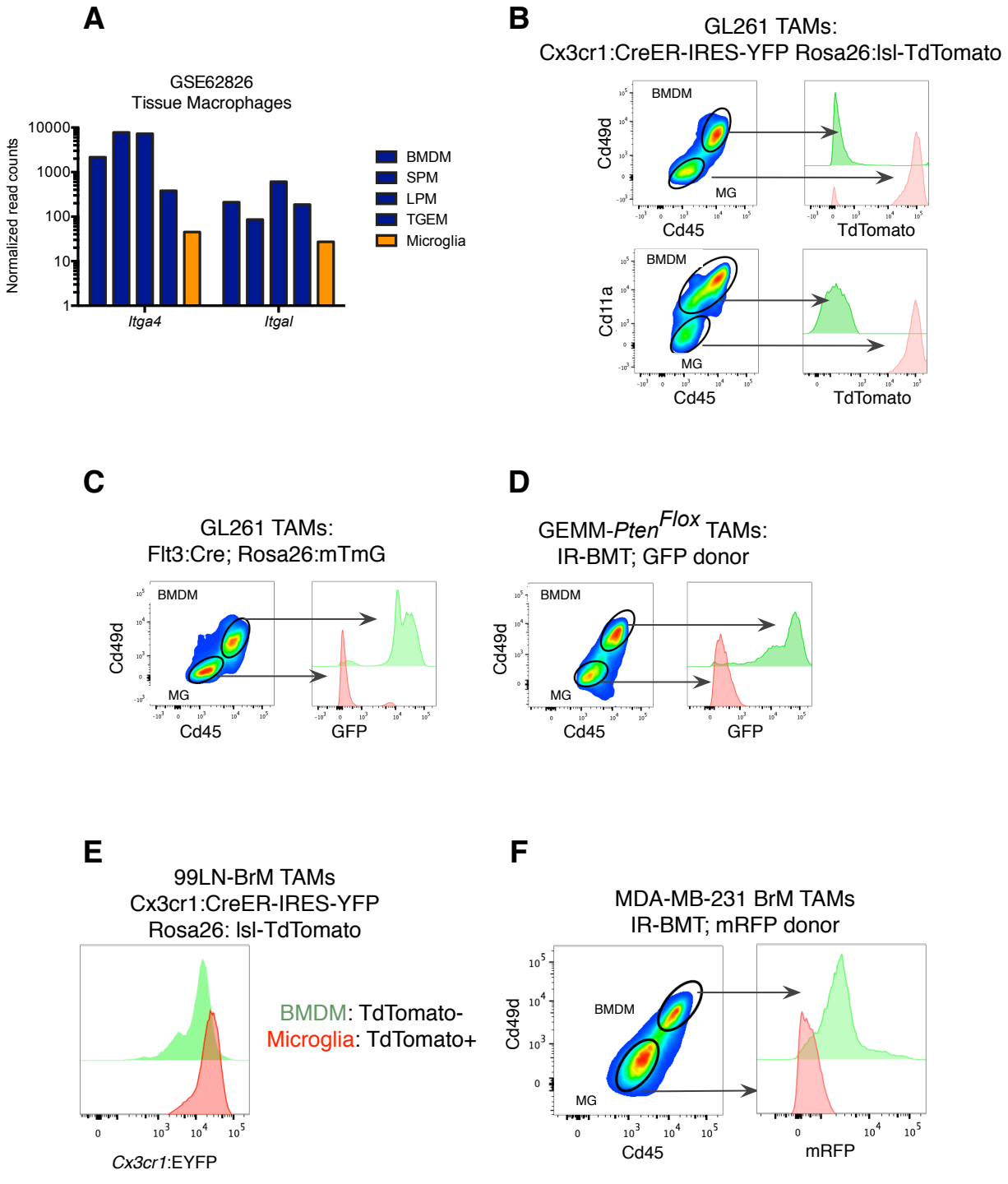
A
GSE62826
Tissue Macrophages
Normalized read counts
10000
1000
100
10
1
Itga4
Itgal
BMDM
SPM
LPM
TGEM
Microglia
B
GL261 TAMs:
Cx3cr1:CreER-IRES-YFP Rosa26:lsl-TdTomato
BMDM
MG
Cd49d
Cd45
TdTomato
Cd11a
C
GL261 TAMs:
Flt3:Cre; Rosa26:mTmG
GFP
D
GEMM-PtenFlox TAMs:
IR-BMT; GFP donor
E
99LN-BrM TAMs
Cx3cr1:CreER-IRES-YFP
Rosa26: lsl-TdTomato
Cx3cr1:EYFP
BMDM: TdTomato-
Microglia: TdTomato+
F
MDA-MB-231 BrM TAMs
IR-BMT; mRFP donor
mRFP

Supplemental Figure 4: Cd49d and Cd11a are enriched in TAM BMDM compared to TAM MG in multiple mouse models of brain malignancy. Related to Figure 4.

(A) Barchart indicating normalized gene read counts from GSE62826 for *Itga4* and *Itgal* in BMDM, small peritoneal macrophages (SPM), large peritoneal macrophages (LPM), thyoglycolate elicited peritoneal macrophages (TGEM), and microglia. Log10 y-axis as indicated. **(B)** Flow cytometry for Cd45 and either Cd49d (top) or Cd11a (bottom) on TAMs isolated from GL261 tumors in Cx3cr1:CreER-IRES-YFP Rosa26:lslTdTomato mice. The adjacent histogram depicts TdTomato expression in the indicated populations. **(C)** As in (B), but for the Flt3:Cre Rosa26:mTmG GL261 model. **(D)** Flow cytometry for Cd45 and Cd49d on TAMs isolated from a $Pten^{flox}$-GEMM tumor in a mouse that underwent IR-BMT reconstituted with GFP^+ donor cells. The adjacent histogram shows GFP expression in the indicated populations. **(E)** Histogram of eYFP expression in $TdTomato^-$ BMDM and $TdTomato^+$ MG from 99LN-BrM brain metastasis in the Cx3cr1:CreER-IRES-YFP Rosa26:lslTdTomato lineage tracing model. **(F)** Flow cytometry and associated histogram for Cd45 and Cd49d on TAMs isolated from a representative MDA-MD-231 xenograft brain metastasis in a IR-BMT mouse reconstituted with mRFP donor cells. The adjacent histogram depicts mRFP expression in the indicated populations. All flow plots are representative of n=5-8 mice.

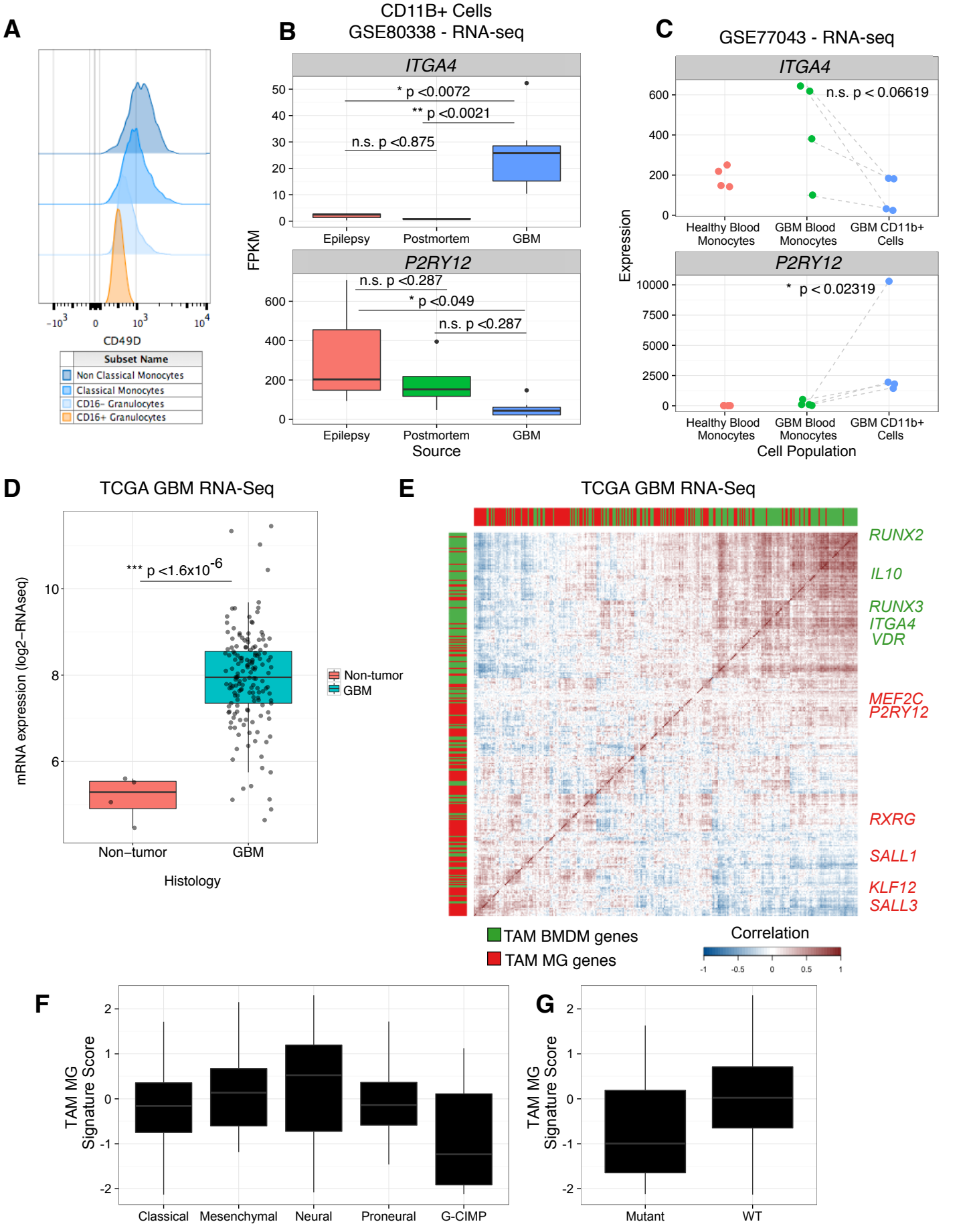
A
CD49D
Subset Name
Non Classical Monocytes
Classical Monocytes
CD16- Granulocytes
CD16+ Granulocytes
B
CD11B+ Cells
GSE80338 - RNA-seq
ITGA4
* p <0.0072
** p <0.0021
n.s. p <0.875
P2RY12
n.s. p <0.287
* p <0.049
n.s. p <0.287
FPKM
Epilepsy
Postmortem
GBM
Source
C
GSE77043 - RNA-seq
ITGA4
n.s. p < 0.06619
P2RY12
* p < 0.02319
Expression
Healthy Blood Monocytes
GBM Blood Monocytes
GBM CD11b+ Cells
Cell Population
D
TCGA GBM RNA-Seq
*** p <1.6x10-6
mRNA expression (log2-RNAseq)
Non-tumor
GBM
Histology
E
TCGA GBM RNA-Seq
RUNX2
IL10
RUNX3
ITGA4
VDR
MEF2C
P2RY12
RXRG
SALL1
KLF12
SALL3
TAM BMDM genes
TAM MG genes
Correlation
F
TAM MG Signature Score
Classical
Mesenchymal
Neural
Proneural
G-CIMP
G
TAM MG Signature Score
Mutant
WT

Supplemental Figure 5: *ITGA4* and markers of TAM BMDM are present in purified cell types and in whole tumor expression data from patients. Related to Figure 5.

(A) Histogram of CD49D expression in non-classical monocytes ($CD45^+CD11B^+CD66B^-CD16^+CD14^{low}$), classical monocytes ($CD45^+CD11B^+CD66B^-CD16^-CD14^+$), $CD16^-$ granulocytes ($CD45^+CD11B^+CD66B^+CD16^-CD14^{low}$) and $CD16^+$ granulocytes ($CD45^+CD11B^+CD66B^+CD16^+CD14^{low}$) from human healthy donor blood. Representative of n=6 samples. **(B)** Boxplot of FPKM (Fragments Per Kilobase of transcript per Million mapped reads) values from GSE80338 dataset for *ITGA4* (top) and *P2RY12* (bottom) across the indicated sample sets. (Student's t-test). **(C)** Stripchart of normalized array intensities from GSE77043 dataset for *ITGA4* (top) and *P2RY12* (bottom) across the indicated sample sets. Dashed lines indicate matched samples. (Student's t-test). **(D)** Normalized log2 RNAseq counts from TCGA-GBM dataset for *ITGA4* in non-malignant brain and GBM tissue. (Student's t-test). **(E)** Pairwise correlation matrix of TAM BMDM (green column marks) and TAM MG (red column marks) genes from the TCGA-GBM RNA-seq dataset. Blue indicates negative correlation between gene pairs and red indicates positive correlation. **(F-G)** Z-scored TAM MG signature scores across (F) tumor subtype (ANOVA $p \leq 0.041$), and (G) *IDH1* mutation status (Student's t-test $p \leq 0.153$). n.s. denotes non-significant p value, * $p \leq 0.05$, ** $p \leq 0.005$, *** $p \leq 0.0005$.

SUPPLEMENTAL EXPERIMENTAL PROCEDURES

Mouse models and cell lines

Mice

Flk2-switch (*Flt3*:Cre, Rosa26:mTmG) mice were kindly provided by Dr. Camilla Forsberg (UCSC) (Benz et al., 2008; Boyer et al., 2011; Muzumdar et al., 2007). Only male mice showed expression or transmittance of Cre, and as such only male mice could be used for these experiments. *Cx3cr1*:CreER-IRES-YFP mice were obtained from Jackson Labs and bred to Rosa26:lsl-TdTomato reporter mice (Jackson Labs) (Madisen et al., 2010; Parkhurst et al., 2013). Nestin:Tva (nTva) mice in a mixed background, as described previously, were bred to C57BL/6 background for 10 generations (Holland et al., 1998; Quail et al., 2016). *Pten*$^{Flox/Flox}$ mice (C57BL/6 background) were obtained from Dr. Charles Sawyers and Dr. Brett Carver (MSKCC) (Trotman et al., 2003). CAG:GFP mice (Okabe et al., 1997) were obtained from Jackson labs. Athymic nude mice were obtained from NCI Frederick and maintained at MSKCC. CAG:RFP mice (Long et al., 2005) were obtained from Jackson labs and crossed to Athymic nude mice for 10 generations. All animal procedures and studies were approved by the MSKCC Institutional Animal Care and Use Committee (protocol 04-08-022).

Brain tumor models

For the glioma models, intracranial injections were performed on 5-6 week old mice as previously described (Pyonteck et al., 2013). Briefly, mice were fully anesthetized with

ketamine/xylazine and bupivacaine was applied as a local anesthetic. Using a stereotactic apparatus, cells were injected into the right frontal cortex (1 mm caudal, 1.5 mm lateral from bregma, 2-3 mm deep). For the GEMM-shP53 model, $3x10^5$ DF1 cells (1:1 mixture of DF1: RCAS-PDGFB-HA, and DF1:RCAS:shP53) were injected at 6 weeks of age. For the GEMM-$Pten^{flox}$ model, $3x10^5$ cells were injected (1:1 mixture of DF1:RCAS-PDGFB-HA and DF1:RCAS-Cre) at 8 weeks of age, 4 weeks after bone marrow transplantation. For the GL261 model, $2x10^4$ cells were injected at 6 weeks of age, or 8 weeks of age if in the *Cx3cr1*:CreER-IRES-YFP lineage tracing background, 3 weeks after tamoxifen administration.

For brain metastasis models, 6-8 week old athymic nude mice or C57BL/6 mice were intracardially injected with $1x10^4$ MDA-BrM cells or 99LN-BrM cells respectively, as previously described (Bos et al., 2009; Sevenich et al., 2014). For the 99LN-BrM model in the *Cx3cr1*:CreER-IRES-YFP lineage tracing background, mice were injected with tamoxifen at 4 weeks of age, and then intracardially injected 3 weeks later, at 7 weeks of age.

Cells

DF1 chicken fibroblasts were obtained from the ATCC. RCAS vectors expressing PDGFB-HA, Cre or a short hairpin against mouse *p53* (shP53) were kindly provided by Dr. Tatsuya Ozawa and Dr. Eric Holland (Ozawa et al., 2014). GL261 murine glioma cells were kindly provided by Dr. Sal Coniglio and Dr. Jeff Segall (Albert Einstein). MDA-MB-231 brain-homing variant cells (MDA-BrM) were kindly provided by Dr. Joan Massague (MSKCC) and labeled with a triple imaging vector (Tk-GFP-Luc) as

previously described (Bos et al., 2009; Ponomarev et al., 2004; Sevenich et al., 2014). 99LN cells were derived from a metastatic lesion in the lymph node of the MMTV:PyMT genetically engineered breast cancer model (C57BL/6 background). Cells were screened *in vitro* for their invasive capacity in a transwell assay, passaged once *in vivo* in a C57BL/6 mouse and selected *in vivo* for their brain homing capacity as described previously for the MDA-MB-231 BrM variant (Bos et al., 2009). All cell lines were maintained in DMEM with 10% fetal bovine serum with penicillin and streptomycin.

Tamoxifen lineage tracing and bone marrow transplantation

For the Cx3cr1:CreER-IRES-YFP Rosa26:lsl-TdTomato lineage tracing system, 4 week-old mice were injected twice, 48 hours apart, i.p. with 1 mg of tamoxifen citrate dissolved in corn oil. Mice were used for intracranial injection of DF1 cells 3 weeks after tamoxifen administration. For bone marrow transplantation, recipient mice were irradiated (Gammacell-40 Exator) with a split dose scheme of 2x4.5 Gy with a window of 4 hours between doses. Whole bone marrow was isolated from the femurs of a CAG:GFP donor mouse (6-8 weeks old) and $1x10^6$ cells were injected i.v. into previously irradiated recipients. Athymic nude mice were irradiated with a split dosage scheme of 2x4 Gy, and were reconstituted using Athymic CAG:RFP donor cells. Experimental mice were intracranially injected with DF1 cells or intracardially injected with MDA-BrM cells 4 weeks after bone marrow transplantation.

Flow cytometry and immunohistochemistry

All antibodies for flow cytometry were titrated in a lot-dependent manner and used as follows: anti-mouse Cd45 (Biolegend 103128), anti-mouse/human Cd11b (BD Biosciences 563553), anti-mouse Ly6C (Biolegend 128026), anti-mouse Ly6G (BD Biosciences 563005), anti-mouse Cd49d (Biolegend 103618), anti-mouse Cd11a (Biolegend 101120), anti-human CD45 (Biolegend 304042), anti-human CD66B (Biolegend 305106), anti-human CD14 (Biolegend 325610), anti-human CD16 (Biolegend 302026), and anti-human CD49D (Biolegend 304308).

For tissue collection for histology, mice were anesthetized with 1.25% Avertin, and transcardially perfused with PBS and 4% paraformaldehyde (PFA). Tissues were macrodissected and the brain was post fixed in 4% PFA overnight and then placed in sucrose, while the spleen was immediately placed in 30% sucrose. Tissue was transferred to 30% sucrose for 2 days, embedded in OCT, and 10 μM cryosections were cut. Immunofluorescence staining followed. First, slides were rehydrated with two washes of PBS for 5 minutes. Tissue was then permeabilized with 0.2% Triton-X in PBS and washed twice with PBS for 5 minutes. Hydrophobic circles were drawn around tissue sections, followed by 2 more washes with PBS for 5 minutes. Tissue was blocked with 0.5% PNB blocking buffer. Primary antibody was applied in 0.25% PNB blocking buffer overnight at 4 degrees Celsius. Tissues were washed 3 times with PBS for 5 minutes. Secondary antibody was applied (1:500, Molecular Probes) for 1 hour at room temperature followed by 3 washes of PBS for 5 minutes. Slides were counterstained with DAPI (1:5000, Molecular Probes) for 5 minutes at room

temperature, washed 3 times with PBS, and mounted with Dako fluorescent mounting media. Primary antibodies used were: chicken-anti GFP (AbCam 13970, 1:500), rat anti-Cd68 (Serotec MCA1957, 1:500), and rabbit anti-Iba1 (Wako, 01-1974, 1:500). Endogenous TdTomato was visible without immunofluorescence staining from both the Rosa26:mTmG and Rosa26:lsl-TdTomato reporter mice. When combined with Cd68 staining (Figure 1J, Figure 2D), the TdTomato signal was assessed using a filter set centered around 546nm, with negligible signal present in the 594nm filter set used to collect the Cd68 signal. Images were obtained on a Zeiss Z1 AxioImager equipped with a TissueGnostics stage. Tiling images were acquired at 20x magnification using TissueFAXS (Tissuegnostics). Single images at 20x and 40x were either acquired using Axiovision (Zeiss), or extracted as single images from the TissueFAXS tiling image acquisition application (for representative images shown in Figure 1C, 1F, 1J, 2D and 4D).

External dataset download and analysis

All TCGA data was analyzed using the web-portal Gliovis (http://gliovis.bioinfo.cnio.es). Normalized gene expression data for the Immunological Genome Project (ImmGen) was obtained from the GEO under accession GSE15907 (Gautier et al., 2012). RNA-seq, ATAC-Seq and ChIP-Seq datasets for tissue resident macrophage transcriptional and epigenetic profiling were downloaded from the SRA using the NCBI SRA-toolkit from the following GEO accession numbers: GSE62826, GSE63338, and GSE63339 (Gosselin et al., 2014; Lavin et al., 2014). RNA-sequencing data on microglia and peripherally-derived macrophages in the non-malignant brain were downloaded under

accession number GSE68376 (Bruttger et al., 2015). Each of these datasets was mapped to the mouse genome mm10 as described above. For ChIP-seq and ATAC-seq datasets the STAR parameter "--alignIntronMax" was set to 1. PU.1 ChIP-Seq peak calling was performed with HOMER (Heinz et al., 2010). Peaks were considered within a promoter if they fell within 2kb upstream or 0.5kb downstream of the nearest transcription start site. Enhancer regions were considered up to 50kb upstream and downstream of the nearest transcription start site, excluding the promoter region. Deeptools was used to assess ChIP-seq and ATAC-seq density over the indicated windows surrounding either transcription start sites, or PU.1 binding sites within enhancers (Ramirez et al., 2014). The findPeaks script with HOMER was used to identify peaks for PU.1 binding with default parameters. The annotatePeaks.pl scripts in the HOMER suite was used to find enriched motifs in ChIP-seq peaks and in gene sets identified through RNA-sequencing. For promoter motif enrichment, only known motifs were considered in regions 300bp upstream and 50bp downstream of the transcription start site.

Transcription factor activity analysis:

Transcription factor (TF) activity analysis was performed as an adaptation of two previously published methods: RegulatorInference (Setty et al., 2012) and ISMARA (Balwierz et al., 2014). Briefly, a set of transcription factor binding sites (TFBS) was screened across the promoters (500bp upstream and 50bp downstream of the transcription start site) of each gene present in the mouse genome (mm10). TFBS were predicted from known motifs provided by HOMER. The AnnotatePeaks.pl script in

HOMER was used to make presence and absence calls for each TFBS in each promoter region. This was then tabulated into a matrix with TFBS motifs as columns and genes as rows. This tabulated matrix was used in a ridge regression to model log2 gene expression values generated by 'varianceStabilizingTransformation' function in the DESeq2 package in R. The glmnet function in R was used to perform the ridge regression. Lambda, the regularization parameter, was determined for each sample by 10-fold cross validation (Friedman et al., 2010). The model coefficients for each TFBS motif were z-scored. Differentially enriched TFBS motifs were determined by evaluating the z-scored values in limma with a fold change cutoff of +/-2 and a false discovery rate of 5% (Ritchie et al., 2015).

Statistical analysis and graph generation:

All statistical analyses were completed using R (version 3.0.1), GraphPad Prism Pro v6, Gliovis (http://gliovis.bioinfo.cnio.es/) or as indicated in the bioinformatics section of the methods. Heatmaps were drawn with the ggplot2, gplots (Warnes et al., 2015) packages in R. Flow cytometry biplots and histograms were plotted in FlowJo v10.8. ATAC-sequencing tracks were visualized in IGV v2.3.66. Venn diagrams were drawn with the VennDiagram (Chen, 2015) and Vennerable (Swinton) packages in R. All other scatterplots, barplots, and boxplots were plotted with the ggplot2 package in R or with GraphPad Prism Pro v6. All boxplots are depicted as Tukey-boxplots with median values, boxes indicating 25% and 75%, and whiskers extending to 1.5 times the interquartile range. All code used in this study can be found at the following website: https://bitbucket.org/bowmanr/joycelab-brain-tme.

SUPPLEMENTAL REFERENCES

Balwierz, P.J., Pachkov, M., Arnold, P., Gruber, A.J., Zavolan, M., and van Nimwegen, E. (2014). ISMARA: automated modeling of genomic signals as a democracy of regulatory motifs. *Genome Research* 24, 869-884.

Benz, C., Martins, V.C., Radtke, F., and Bleul, C.C. (2008). The stream of precursors that colonizes the thymus proceeds selectively through the early T lineage precursor stage of T cell development. *The Journal of Experimental Medicine* 205, 1187-1199.

Bos, P.D., Zhang, X.H., Nadal, C., Shu, W., Gomis, R.R., Nguyen, D.X., Minn, A.J., van de Vijver, M.J., Gerald, W.L., Foekens, J.A., and Massague, J. (2009). Genes that mediate breast cancer metastasis to the brain. *Nature* 459, 1005-1009.

Boyer, S.W., Schroeder, A.V., Smith-Berdan, S., and Forsberg, E.C. (2011). All hematopoietic cells develop from hematopoietic stem cells through Flk2/Flt3-positive progenitor cells. *Cell Stem Cell* 9, 64-73.

Bruttger, J., Karram, K., Wortge, S., Regen, T., Marini, F., Hoppmann, N., Klein, M., Blank, T., Yona, S., Wolf, Y., et al. (2015). Genetic cell ablation reveals clusters of local self-renewing microglia in the mammalian central nervous system. *Immunity* 43, 92-106.

Chen, H. (2015). VennDiagram: generate high-resolution Venn and Euler plots.

Friedman, J., Hastie, T., and Tibshirani, R. (2010). Regularization paths for generalized linear models via coordinate descent. *Journal of Statistical Software* 33, 1-22.

Gautier, E.L., Shay, T., Miller, J., Greter, M., Jakubzick, C., Ivanov, S., Helft, J., Chow, A., Elpek, K.G., Gordonov, S., et al. (2012). Gene-expression profiles and transcriptional regulatory pathways that underlie the identity and diversity of mouse tissue macrophages. *Nature Immunology* 13, 1118-1128.

Gosselin, D., Link, V.M., Romanoski, C.E., Fonseca, G.J., Eichenfield, D.Z., Spann, N.J., Stender, J.D., Chun, H.B., Garner, H., Geissmann, F., and Glass, C.K. (2014). Environment drives selection and function of enhancers controlling tissue-specific macrophage identities. *Cell* 159, 1327-1340.

Heinz, S., Benner, C., Spann, N., Bertolino, E., Lin, Y.C., Laslo, P., Cheng, J.X., Murre, C., Singh, H., and Glass, C.K. (2010). Simple combinations of lineage-determining transcription factors prime cis-regulatory elements required for macrophage and B cell identities. *Molecular Cell* 38, 576-589.

Holland, E.C., Hively, W.P., DePinho, R.A., and Varmus, H.E. (1998). A constitutively active epidermal growth factor receptor cooperates with disruption of G1 cell-cycle arrest pathways to induce glioma-like lesions in mice. *Genes & Development* 12, 3675-3685.

Lavin, Y., Winter, D., Blecher-Gonen, R., David, E., Keren-Shaul, H., Merad, M., Jung, S., and Amit, I. (2014). Tissue-resident macrophage enhancer landscapes are shaped by the local microenvironment. *Cell* 159, 1312-1326.

Long, J.Z., Lackan, C.S., and Hadjantonakis, A.K. (2005). Genetic and spectrally distinct in vivo imaging: embryonic stem cells and mice with widespread expression of a monomeric red fluorescent protein. *BMC Biotechnology* 5, 20.

Madisen, L., Zwingman, T.A., Sunkin, S.M., Oh, S.W., Zariwala, H.A., Gu, H., Ng, L.L., Palmiter, R.D., Hawrylycz, M.J., Jones, A.R., et al. (2010). A robust and high-throughput Cre reporting and characterization system for the whole mouse brain. *Nature Neuroscience* 13, 133-140.

Muzumdar, M.D., Tasic, B., Miyamichi, K., Li, L., and Luo, L. (2007). A global double-fluorescent Cre reporter mouse. *Genesis* 45, 593-605.

Okabe, M., Ikawa, M., Kominami, K., Nakanishi, T., and Nishimune, Y. (1997). 'Green mice' as a source of ubiquitous green cells. *FEBS Letters* 407, 313-319.

Ozawa, T., Riester, M., Cheng, Y.K., Huse, J.T., Squatrito, M., Helmy, K., Charles, N., Michor, F., and Holland, E.C. (2014). Most human non-GCIMP glioblastoma subtypes evolve from a common proneural-like precursor glioma. *Cancer Cell* 26, 288-300.

Parkhurst, C.N., Yang, G., Ninan, I., Savas, J.N., Yates, J.R., 3rd, Lafaille, J.J., Hempstead, B.L., Littman, D.R., and Gan, W.B. (2013). Microglia promote learning-dependent synapse formation through brain-derived neurotrophic factor. *Cell* 155, 1596-1609.

Ponomarev, V., Doubrovin, M., Serganova, I., Vider, J., Shavrin, A., Beresten, T., Ivanova, A., Ageyeva, L., Tourkova, V., Balatoni, J., et al. (2004). A novel triple-modality reporter gene for whole-body fluorescent, bioluminescent, and nuclear noninvasive imaging. *European Journal of Nuclear Medicine and Molecular Imaging* 31, 740-751.

Pyonteck, S.M., Akkari, L., Schuhmacher, A.J., Bowman, R.L., Sevenich, L., Quail, D.F., Olson, O.C., Quick, M.L., Huse, J.T., Teijeiro, V., et al. (2013). CSF-1R inhibition alters macrophage polarization and blocks glioma progression. *Nature Medicine* 19, 1264-1272.

Quail, D.F., Bowman, R.L., Akkari, L., Quick, M.L., Schuhmacher, A.J., Huse, J.T., Holland, E.C., Sutton, J.C., and Joyce, J.A. (2016). The tumor microenvironment underlies acquired resistance to CSF-1R inhibition in gliomas. Science *352*, aad3018.

Ramirez, F., Dundar, F., Diehl, S., Gruning, B.A., and Manke, T. (2014). deepTools: a flexible platform for exploring deep-sequencing data. *Nucleic Acids Research* 42, W187-191.

Ritchie, M.E., Phipson, B., Wu, D., Hu, Y., Law, C.W., Shi, W., and Smyth, G.K. (2015). limma powers differential expression analyses for RNA-sequencing and microarray studies. *Nucleic Acids Research* 43, e47.

Setty, M., Helmy, K., Khan, A.A., Silber, J., Arvey, A., Neezen, F., Agius, P., Huse, J.T., Holland, E.C., and Leslie, C.S. (2012). Inferring transcriptional and microRNA-mediated regulatory programs in glioblastoma. *Molecular Systems Biology* 8, 605.

Sevenich, L., Bowman, R.L., Mason, S.D., Quail, D.F., Rapaport, F., Elie, B.T., Brogi, E., Brastianos, P.K., Hahn, W.C., Holsinger, L.J., et al. (2014). Analysis of tumour- and stroma-supplied proteolytic networks reveals a brain-metastasis-promoting role for cathepsin S. *Nature Cell Biology* 16, 876-888.

Swinton, J. Vennerable: Venn and Euler area-proportional diagrams.

Trotman, L.C., Niki, M., Dotan, Z.A., Koutcher, J.A., Di Cristofano, A., Xiao, A., Khoo, A.S., Roy-Burman, P., Greenberg, N.M., Van Dyke, T., et al. (2003). Pten dose dictates cancer progression in the prostate. *PLoS Biology* 1, E59.

Warnes, G.R., Bolker, B., Bonebakker, L., Gentleman, R., Huber, W., Liaw, A., Lumley, T., Maechler, M., Magnusson, A., Moeller, S., et al. (2015). gplots: Various R Programming Tools for Plotting Data.